Wave Driven Free Surface Motion in the Gap between a Tanker and an FLNG Barge

L. Sun[a], R. Eatock Taylor[*a,b] and P. H. Taylor[b]

[a] Centre for Offshore Research & Engineering and Department of Civil & Environmental Engineering, National University of Singapore, No.1 Engineering Drive 2, Singapore 117576
[b] Department of Engineering Science, University of Oxford, Parks Road, Oxford OX1 3PJ, UK

Abstract

When two vessels are moored side-by-side with a narrow gap between them, intense free surface motions may be excited in the gap as a result of complex hydrodynamic interactions. These influence the motions of the two vessels, and the forces in any moorings. The present paper uses first and second order wave diffraction analysis to investigate this phenomenon. Key theoretical aspects of the numerical analysis are first summarised, including the vital need to suppress "irregular frequency" effects; and results are given to validate the code used. The case of a tanker alongside a large floating FLNG barge is then considered in detail.

Keywords: Hydrodynamic interactions; closely spaced vessels; gap resonances; second order diffraction.

[*] Corresponding author, email: r.eatocktaylor@eng.ox.ac.uk

1. Introduction

A hydrodynamic issue of crucial importance in the design of Floating Liquid Natural Gas (FLNG) off-loading systems is that of wave induced interactions between the vessels when moored very closely alongside each other (or of a tanker and a gravity-based structure supporting the LNG processing plant). Such interactions can radically change the hydrodynamic forces on the vessel(s) (wave exciting forces, as well as added mass and damping effects), and so modify the motion responses from what would be predicted for the same vessels in isolation. The close proximity of the vessels can also lead to very large free surface motions between them, in head seas as well as beam seas and indeed in waves incident from any direction. As a result, this topic is of considerable current research interest [e.g. 1-5], and has been the focus of major effort in the EU Framework 6 Safe Offload research project. Both experimental and numerical work has been undertaken, and the present paper is concerned with the latter.

Several difficulties arise when one considers appropriate strategies for constructing numerical models. The problem is inherently three dimensional (3D), as is immediately apparent when one observes in experiments the waves generated along the gap between two parallel vessels that are subject to beam seas. The problem can also be expected to be significantly influenced by viscous effects: linked to the roll motions of the vessels responding independently, as well as to potentially violent fluid motions in the gap and in the close vicinity of the hulls. In the future it may be feasible to use a full 3D Navier-Stokes code to resolve these issues in a practical numerical model. Prior to that, however, much may be learnt concerning the behaviour of closely spaced vessels by implementing appropriate potential flow models. In particular, such models can be expected to yield reliable predictions of the frequencies at which strong interactions will arise, and indications of the influence of key parameters such as spacing between the hulls (i.e. gap width), draught and gap length. Furthermore, second order diffraction analysis can clarify the possibilities of strong interaction effects at double frequencies in regular waves (or “sum” and “difference” frequencies in irregular waves). Second order effects would be important if it was found, for example, that a swell with a period of 16 s could excite very large responses with a period of 8s through frequency doubling effects.

In the present work we have implemented such a second order analysis using a frequency domain boundary element model of the two vessels. Preliminary findings for the simple geometry of two closely spaced rectangular boxes have been given by Sun et al. [6]. In that paper, results

were discussed in the context of some very simple analytical solutions (analogous to solutions of the moonpool problem [7]). Here we aim to investigate the phenomenon for the rather more realistic case of an LNG tanker alongside an FLNG barge (albeit still with some simplifications to the geometry). We also provide here some additional details of the boundary element method we have implemented. The latter are described in Section 2 of this paper. Section 3 concerns some examples of its validation, where particular features discussed are the issue of avoiding so-called “irregular frequencies”, and the modelling of multiple bodies which respond independently. The geometry and meshing of the FLNG barge and LNG tanker are reviewed in Section 4, and the results are given in Section 5 followed by some conclusions.

2. Overview of the DIFFRACT model

2.1 Background

The boundary element method (BEM) has proved to be an invaluable technique for modelling linear and nonlinear wave diffraction problems. WAMIT [8, 9] is probably the most sophisticated of the commercially available BEM based codes which can analyze wave diffraction up to second order. DIFFRACT is another second order diffraction code which has been developed for research use over many years [10-13]. It has many similar capabilities to WAMIT, though it is based on a modified integral equation, which avoids the inconvenient representation of the solid angle, which is required in many implementations. For the work described here, this code has been improved and extended, both in terms of flexibility and efficiency of use, and in providing a capability to deal with multiple floating bodies. A feature which has been found to be essential for solving the problems addressed here is the capability of suppressing so-called “irregular frequencies”. These arise when the integral equation is formulated using the wave source Green function. Such a formulation has the advantage in the linear problem that the integral equation only has to be discretised on the submerged surface of the diffracting body. It has the disadvantage, however, that at certain “irregular frequencies” the equation has no unique solution, and the discretised system of equations can be very poorly conditioned near such frequencies. The particular way in which this problem has been overcome in DIFFRACT has not previously been published, and is described below. This requires first some explanation of the integral equations on which first and second order solutions are based in DIFFRACT.

2.2 Governing equations

In the first order analysis, at each component wave frequency ω the linear velocity potential has the form

$$\Phi^{(1)}(x,y,z,t) = \mathrm{Re}\left[\phi^{(1)}(x,y,z)e^{-i\omega t}\right] \tag{1}$$

where Re[ ] means the real part of complex number. The potential has components due to the incident wave (I) and the scattered waves (S). The latter include the wave diffracted by the fixed body (D), and radiated waves due to the combined effects of the body motions (R), so that

$$\phi^{(1)} = \phi_I^{(1)} + \phi_S^{(1)} \text{ where } \phi_S^{(1)} = \phi_D^{(1)} + \phi_R^{(1)}. \tag{2}$$

With the assumption of linearity, we can write the motions of a single rigid body as

$$\vec{\Xi}^{(1)} = \mathrm{Re}[\vec{\xi}^{(1)} e^{-\mathrm{i}\omega t}] \tag{3}$$

where $\vec{\xi}^{(1)}$ is the vector used to define the three translations and three rotations. The radiation potential can then be rewritten as

$$\phi_R^{(1)} = \sum_{m=1}^{6} -i\omega\xi_m^{(1)}\phi_m^{(1)} \qquad (m = 1,2,\cdots,6) \tag{4}$$

If we further define $\phi_0^{(1)} = \phi_I^{(1)}$ and $\phi_7^{(1)} = \phi_D^{(1)}$, the first order potential has the form of

$$\phi^{(1)} = \phi_0^{(1)} + \sum_{m=1}^{6} -i\omega\xi_m^{(1)}\phi_m^{(1)} + \phi_7^{(1)} \tag{5}$$

The unknown potentials $\phi_m^{(1)}$ (m=1,2, ….., 7) in the above Eq. (5) satisfy the usual boundary conditions on the mean external free surface S_{Fe} and the sea bottom, and the conditions at infinity; and the diffraction and radiation potentials satisfy appropriate conditions on the equilibrium body surface S_B.

In the boundary element analysis we use a Green function $G^{(1)}(\vec{x},\vec{x}_0)$ satisfying the linear free surface and seabed boundary conditions and the Sommerfeld radiation boundary condition:

$$G^{(1)}(\vec{x},\vec{x}_0) = -\frac{1}{4\pi}\left[\frac{1}{r}+\frac{1}{r_2}+2\int_0^\infty \frac{(\mu+\nu)e^{-\mu h}\cosh\left[\mu(z_0+h)\right]\cosh\left[\mu(z+h)\right]}{\mu\sinh(\mu h)-\nu\cosh(\mu h)} J_0(\mu R)d\mu\right] \tag{6}$$

in which $\nu = \omega^2/g$, $\vec{x} = (x,y,z)$ are the coordinates of the field point, $\vec{x}_0 = (x_0, y_0, z_0)$ are the coordinates of the source point and h is the water depth, $R = \sqrt{(x-x_0)^2+(y-y_0)^2}$, $r = \sqrt{R^2+(z-z_0)^2}$, $r_2 = \sqrt{R^2+(z+2h+z_0)^2}$. Here $J_0(\mu R)$ denotes the zero order Bessel function of the first kind and μ is the Fourier transform variable. This leads to the commonly used integral equation for the potential $\phi_m^{(1)}$

$$C(\vec{x}_0)\phi_m^{(1)}(\vec{x}_0) + \iint_{S_B}\phi_m^{(1)}(\vec{x})\frac{\partial G^{(1)}}{\partial \vec{n}}ds = \iint_{S_B} G^{(1)}V_m^{(1)}(\vec{x})ds, \tag{7}$$

where $V_7^{(1)}(\vec{x}) = -\dfrac{\partial\phi_I^{(1)}(\vec{x})}{\partial\vec{n}}$ for the diffraction potential and $V_m^{(1)}(\vec{x}) = n_m$ (n_m is the m^{th} component of the generalized normal vector) for the m^{th} radiation potential. Here $C(\vec{x}_0)$ has the value 1 when $\vec{x}_0$ is in the fluid domain and 1/2 when $\vec{x}_0$ is on the equilibrium body surface S_B as long as the body surface is smooth. For a non-smooth surface, the value of $C(\vec{x}_0)$ will be associated with the exterior solid angle at a surface discontinuity. The discontinuity in the value of $C(\vec{x}_0)$ can cause difficulties in solving the above integral equation near to the body and the integrand has a singularity associated with it. The approach used by Chau [14] showed that this can be overcome by applying Green's theorem to the region interior to the body, bounded by the equilibrium body surface and an inner free surface S_{Fi}. In DIFFRACT a modified integral equation is used, of the form

$$\left(1-\nu\iint_{S_{Fi}} G^{(1)}ds\right)\phi_m^{(1)}(\vec{x}_0) + \iint_{S_B}\left(\phi_m^{(1)}(\vec{x})-\phi_m^{(1)}(\vec{x}_0)\right)\frac{\partial G^{(1)}}{\partial\vec{n}}ds = \iint_{S_B} G^{(1)}V_m^{(1)}(\vec{x})ds \tag{8}$$

The function $C(\vec{x}_0)$ has been removed from the integral equation and the integrand is now non-singular. Eq. (8) is discretised, and the unknown potentials $\phi_m^{(1)}$ solved from the matrix equations. Wave excitation forces and hydrodynamic coefficients are calculated by the integration of pressures on the equilibrium body surface. The response of the floating body $\vec{\xi}^{(1)}$ is obtained by solving the

motion equations. Then $\phi^{(1)}$ and $\phi_S^{(1)}$ which are used in the second order analysis are evaluated from Eqs. (2) and (4).

Next we consider the second order problem. The complete wave velocity potential to second order can be expanded using Stokes' perturbation method as

$$\Phi(x,y,z,t) = \mathrm{Re}\left[\sum_{j=1}^{N}\phi_j^{(1)}(x,y,z)e^{-i\omega_j t} + \sum_{j=1}^{N}\sum_{l=1}^{N}[\phi_{jl}^{+}(x,y,z)e^{-i\omega_{jl}^{+}t} + \phi_{jl}^{-}(x,y,z)e^{-i\omega_{jl}^{-}t}]\right] \tag{9}$$

Here ω_j is the j^{th} wave frequency, and N is the total number of frequency components. The sum and difference frequency components are

$$\omega_{jl}^{+} = \omega_j + \omega_l\,, \quad \omega_{jl}^{-} = \omega_j - \omega_l\,.$$

The second order diffraction potentials $\phi_D^{\pm}$ then satisfy:

$$\frac{\partial^2\phi_D^{\pm}}{\partial x^2} + \frac{\partial^2\phi_D^{\pm}}{\partial y^2} + \frac{\partial^2\phi_D^{\pm}}{\partial z^2} = 0 \qquad \text{in the fluid domain } \Omega \tag{10}$$

$$\frac{\partial\phi_D^{\pm}}{\partial\vec{n}} = -\frac{\partial\phi_I^{\pm}}{\partial\vec{n}} + F_B^{\pm} \qquad \text{on } S_B \tag{11}$$

$$\frac{\partial\phi_D^{\pm}}{\partial z} = 0 \qquad \text{on the seabed} \tag{12}$$

$$\frac{\partial\phi_D^{\pm}}{\partial z} - \frac{\omega^{\pm}}{g}\phi_D^{\pm} = F^{\pm} \qquad \text{on the external free surface} \tag{13}$$

together with a radiation condition. The term $F_B^{\pm}$ on the equilibrium body surface incorporates the terms due to products of its first order motions, and is defined by:

$$F_B^{\pm} = \vec{n}\cdot\vec{w}^{\pm}\,. \tag{14}$$

The sum frequency second order motion is

$$\vec{w}^{+} = \frac{1}{4}\Big[-i(\omega_j + \omega_l)\Big(\big[H^{+}\big]_{lj} + \big[H^{+}\big]_{jl}\Big)\vec{r}$$
$$+\vec{\alpha}_j^{(1)} \times \Big(i\omega_l \vec{\chi}_l^{(1)} + \nabla\phi_l^{(1)}\Big) + \vec{\alpha}_l^{(1)} \times \Big(i\omega_j \vec{\chi}_j^{(1)} + \nabla\phi_j^{(1)}\Big) \tag{15}$$
$$-\Big(\vec{\chi}_j^{(1)} \cdot \nabla\Big)\nabla\phi_l^{(1)} - \Big(\vec{\chi}_l^{(1)} \cdot \nabla\Big)\nabla\phi_j^{(1)}\Big]$$

where $\phi_j^{(1)}$ now represents the total first order potential at frequency *j*, and similarly for $\phi_l^{(1)}$. It is convenient to write the displacements in the form

$$\vec{\chi}_j^{(1)} = \vec{\xi}_j^{(1)} + \vec{\alpha}_j^{(1)} \times \vec{r}\,, \quad \vec{\chi}_l = \vec{\xi}_l^{(1)} + \vec{\alpha}_l^{(1)} \times \vec{r}\,, \tag{16}$$

where $\vec{\xi} = (\xi_1^{(1)}, \xi_2^{(1)}, \xi_3^{(1)})$ are the translational motions and $\vec{\alpha} = (\xi_4^{(1)}, \xi_5^{(1)}, \xi_6^{(1)})$ are rotations. Furthermore,

$$\big[H^{+}\big]_{lj} + \big[H^{+}\big]_{jl} = -\begin{bmatrix} \xi_{5j}^{(1)}\xi_{5l}^{(1)} + \xi_{6j}^{(1)}\xi_{6l}^{(1)} & 0 & 0 \\ -\xi_{4j}^{(1)}\xi_{5l}^{(1)} - \xi_{4l}^{(1)}\xi_{5j}^{(1)} & \xi_{4j}^{(1)}\xi_{4l}^{(1)} + \xi_{6j}^{(1)}\xi_{6l}^{(1)} & 0 \\ -\xi_{4j}^{(1)}\xi_{6l}^{(1)} - \xi_{4l}^{(1)}\xi_{6j}^{(1)} & -\xi_{5j}^{(1)}\xi_{6l}^{(1)} - \xi_{5l}^{(1)}\xi_{6j}^{(1)} & \xi_{4j}^{(1)}\xi_{4l}^{(1)} + \xi_{5j}^{(1)}\xi_{5l}^{(1)} \end{bmatrix}. \tag{17}$$

The term $F^{\pm}$ occurring in the free surface boundary condition Eq. (13) is the product of linear terms, driving the second order diffraction field due to the presence of the structure. The sum-frequency component F^{+} is given by

$$F^{+} = \frac{-i\omega_j}{2g}\phi_{Sj}^{(1)}\Big(\frac{-\omega_l^2}{g}\frac{\partial\phi_l^{(1)}}{\partial z} + \frac{\partial^2\phi_l^{(1)}}{\partial z^2}\Big) - \frac{i\omega_l}{2g}\phi_{Sl}^{(1)}\Big(\frac{-\omega_j^2}{g}\frac{\partial\phi_j^{(1)}}{\partial z} + \frac{\partial^2\phi_j^{(1)}}{\partial z^2}\Big)$$
$$-\frac{i\omega_j}{2g}\phi_{Ij}^{(1)}\Big(\frac{-\omega_l^2}{g}\frac{\partial\phi_{Sl}^{(1)}}{\partial z} + \frac{\partial^2\phi_{Sl}^{(1)}}{\partial z^2}\Big) - \frac{i\omega_l}{2g}\phi_{Il}^{(1)}\Big(\frac{-\omega_j^2}{g}\frac{\partial\phi_{Sj}^{(1)}}{\partial z} + \frac{\partial^2\phi_{Sj}^{(1)}}{\partial z^2}\Big) \tag{18}$$
$$+\frac{i(\omega_j + \omega_l)}{2g}\big(\nabla\phi_{Ij}^{(1)} \cdot \nabla\phi_{Sl}^{(1)} + \nabla\phi_{Sj}^{(1)} \cdot \nabla\phi_{Il}^{(1)} + \nabla\phi_{Sj}^{(1)} \cdot \nabla\phi_{Sl}^{(1)}\big)$$

where $\phi_{Sj}^{(1)}$ and $\phi_{Sl}^{(1)}$ are the scattered velocity potentials, corresponding to frequencies *j* and *l* respectively, and $\phi_{Ij}^{(1)}$ and $\phi_{Il}^{(1)}$ are the incident wave velocity potentials.

The corresponding difference-frequency terms $\vec{w}^-$ and F^- have similar forms, with ω_l replaced by $-\omega_l$ and terms of the form $(a_j b_l + a_l b_j)$ replaced by $(a_j b_l^* + a_l^* b_j)$. An asterisk denotes the complex conjugate.

As with the first order analysis, the solution of the second order sum and difference frequency terms can also be obtained by applying Green's theorem to the fluid domain. The modified integral equation for the second order diffraction potentials is

$$\begin{aligned}&\left(1-\nu^{\pm}\iint_{S_{Fi}} G^{\pm} ds\right)\phi_D^{\pm}(\vec{x}_0) + \iint_{S_B}\left(\phi_D^{\pm}(\vec{x}) - \phi_D^{\pm}(\vec{x}_0)\right)\frac{\partial G^{\pm}}{\partial \vec{n}} ds \\ &= -\iint_{S_B} G^{\pm}\frac{\partial \phi_I^{\pm}}{\partial \vec{n}}(\vec{x}) ds - \iint_{S_{Fe}} F^{\pm}(\vec{x}) G^{\pm} ds + \iint_{S_B} F_B^{\pm}(\vec{x}) G^{\pm} ds\end{aligned} \tag{19}$$

where $\nu^{\pm} = (\omega^{\pm})^2/g$ and $G^{\pm}$ is the Green function for the sum and difference frequency problems (in which ν is replaced by $\nu^{\pm}$).

2.3 Discretisation of the integral equations

Equations (8) and (19) are the underlying integral equations used in the DIFFRACT BEM code, corresponding to the first and second order problems respectively. These are discretised using quadratic isoparametric elements [15]. This leads to a set of matrix equations for the unknown nodal values of velocity potential. Six-node triangular and eight-node quadrilateral elements are used, leading to models in which the velocity potential is assumed to have a quadratic variation over the (curved) elements.

In order to reduce the computational requirements in the case of geometries having one or two planes of symmetry, the matrix equations are reorganised and reduced in size. If for example there is one plane of symmetry, the equation set for the complete problem (e.g. for the 7 unknowns in the diffraction-radiation problem of a single body) is reduced in size by approximately a factor of two. The unknowns are split into symmetric and antisymmetric components, so the number of equations is doubled (to 14 in this example). For two planes of symmetry, the factor is four. Details of the formulation are given in [16]. It should be noted that the approach depends on the symmetry properties of the body geometry: the diffracted wave field will not be symmetric, and waves may propagate at any arbitrary angle to the body.

It can be seen that Eq. (19) involves an additional integral over the exterior free surface S_{Fe}. This is because the Green function $G^{\pm}$ corresponding to frequencies $\omega^{\pm}$ satisfies the homogeneous linear free surface boundary condition rather than the inhomogeneous second order free surface boundary condition, Eq. (13). The integrand $F^{\pm}(\vec{x})G^{\pm}$ involves the product of derivatives of the first-order velocity potentials, as shown in Eq. (18) for example, and is highly oscillatory. It only decays algebraically with increasing distance from the body. In the program DIFFRACT, the external free surface is divided into three domains over which different numerical treatments are implemented. The first region is the inner region S_{Fe1}, where the integration can be evaluated by using quadratic panels defined in a region between the body water line and a circumscribing circle. The second and third regions are the remaining portions of the free surface exterior to the circumscribing circle. In the second region, the integration on the external free surface is replaced by a line integral of individual Fourier harmonics. The third region (from the outer boundary of the second region to infinity) is defined as the far field region where the evanescent components of the scattered waves are assumed to have decayed away and all that remains are radially propagating waves. In the far field region, therefore, the integrand can be approximated by a simple asymptotic formulation, thereby improving the efficiency of the calculation. More details can be found in [14].

2.4 Avoidance of irregular frequencies

The equation set summarized above is well known to be susceptible to the phenomenon of "irregular frequencies". This means a unique solution cannot be obtained at some discrete frequencies. This in turn leads to sharp "jumps" in numerical results in the neighbourhood of these frequencies. These do not originate from physical phenomena; they are a feature of the integral equation. The locations of the discrete irregular frequencies can be determined by theoretical analysis for bodies with simple geometries: they are obtained from the eigenvalues of the boundary value problem for the potential inside the body, subject to the linear free surface condition and a Dirichlet condition of zero potential on the body surface. For complex structures, it is sometimes hard to distinguish whether the results have been polluted by irregular frequencies. Particularly difficult cases are multiple-body problems, because they can show similar "jumps" at resonant frequencies, where strong physical interactions will arise. This is even more serious for second order problems, because correct results can only be achieved if the computations at both second order and first order are all free of irregular frequencies. If for example one is aiming to calculate

second order results in a pair of waves at frequencies ω_1 and ω_2, then one must avoid the possibility of any of the irregular frequencies coinciding with any of ω_1, ω_2, $(\omega_1+\omega_2)$, or $(\omega_1-\omega_2)$.

There are two approaches to avoiding the "irregular frequencies". One is to use other numerical methods which are free of "irregular frequencies", such as a boundary element method using simple Green functions (e.g. $1/r$), or hybrid methods. Another is to remove the "irregular frequencies" by overcoming the lack of uniqueness in the original formulation. We have adopted this latter approach. The implementation is similar to that of Sun et al. [17], though differs in detail. This is because the underlying integral equations which Sun et al. modify to remove irregular frequencies are different from those used here (Eq. (8) at first order and Eq. (19) at second order, designated the "old equations" in what follows).

The code DIFFRACT adopts the following "new equations" for the diffraction problem:

$$\left(1-\nu^{(j)}\iint_{S_{F_i}} G^{(j)}(\vec{x}_0,\vec{x})ds\right)\phi_D^{(j)}(\vec{x}_0)+\iint_{S_B}\left(\phi_D^{(j)}(\vec{x})-\phi_D^{(j)}(\vec{x}_0)\right)\frac{\partial G^{(j)}(\vec{x}_0,\vec{x})}{\partial \vec{n}}ds$$
$$=-\iint_{S_B} G^{(j)}(\vec{x}_0,\vec{x})\frac{\partial \phi_I^{(j)}(\vec{x})}{\partial \vec{n}}ds-\iint_{S_F} F^{(j)}G^{(j)}(\vec{x}_0,\vec{x})+\int\int_{S_B} F_B^{(j)}(\vec{x})G^{(j)}(\vec{x}_0,\vec{x})ds \qquad (\vec{x}_0\in S_B) \tag{20}$$

$$\iint_{S_B}\phi_D^{(j)}(\vec{x})\frac{\partial G^{(j)}(\vec{x}_0,\vec{x})}{\partial \vec{n}}ds$$
$$=-\iint_{S_B} G^{(j)}(\vec{x}_0,\vec{x})\frac{\partial \phi_I^{(j)}(\vec{x})}{\partial \vec{n}}ds-\iint_{S_{F_e}} F^{(j)}G^{(j)}(\vec{x}_0,\vec{x})ds+\int\int_{S_B} F_B^{(j)}(\vec{x})G^{(j)}(\vec{x}_0,\vec{x})ds \qquad (\vec{x}_0\in S_{F_i}) \tag{21}$$

$$\iint_{S_{F_i}}\psi^{(j)}(\vec{x})\frac{\partial G^{(j)}(\vec{x}_0,\vec{x})}{\partial \vec{n}}ds=0 \qquad (\vec{x}_0\in S_B) \tag{22}$$

$$\psi^{(j)}(\vec{x}_0)+\iint_{S_{F_i}}\psi^{(j)}(\vec{x})\frac{\partial G^{(j)}(\vec{x}_0,\vec{x})}{\partial \vec{n}}ds=0 \qquad (\vec{x}_0\in S_{F_i}) \tag{23}$$

Here $\psi^{(j)}$ are nodal potentials on the inner free surface. The equations are written in a compact form to indicate how both the first order (superscript j=1) and the second order (j=2) equations are modified. Here superscript (2) is equivalent to ± above, and $F^{(1)}=0$, $F_B^{(1)}=0$. In the above form, two integral equations (Eq. (20) and (21)) on the equilibrium body surface and two integral equations (Eq. (22) and (23)) on the inner free surface are incorporated. In Eq. (20) and (21), the resulting matrix is over-determined. But these equations are added to Eq. (22) and (23) respectively, leading to a set of matrix equations for the unknowns $\phi^{(j)}$ and $\psi^{(j)}$. The resulting equations have unique solutions at all frequencies.

An important issue relating to the new equations is the incompatibility of the velocity potentials $\phi^{(j)}$ and $\psi^{(j)}$ at the inner water line, the intersection curve of the body surface S_B and the inner free surface S_{Fi}. The value of the velocity potential on the inner water plane must be zero, and that on the body should be non-zero. To avoid this conflict, discontinuous elements are used in discretisation of the integral equations. For all geometric quantities, continuous higher order boundary elements are adopted to simulate the surface of the integration domain. For the physical quantities on the surface of the body and the interior part of the inner water plane, continuous higher order boundary elements are adopted; for the physical quantities on the boundary of the inner water plane, partially discontinuous higher order boundary elements are adopted (as described in [18]). By this means, not only is geometric continuity ensured, but also the physical discontinuity on the interface of the body surface and the inner water plane is retained.

As an example, on the inner water plane of a circular cylinder or hemisphere, the distribution of elements could be as shown in Fig. 1 (in which × represents geometric nodes, and ● represents physical nodes). The distribution of nodes in a partially discontinuous element is shown in Fig. 2, where G1, G2, G3, G4, G5, G6, G7, G8 are geometric nodes; and P1, P2, P3, P4, P5, P6, P7, P8 are physical nodes.

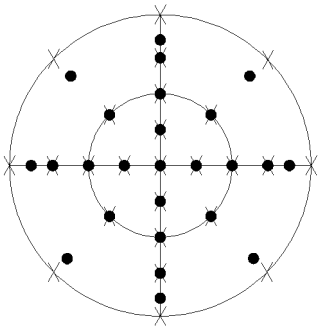

Figure 1. Sketch of elements on the inner water plane

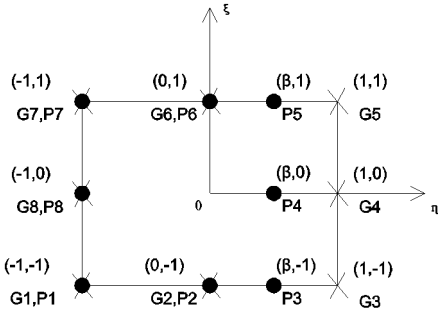

Figure 2. Distribution of nodes in a quadrilateral element, as specified in local coordinates

3. Validation

The implementation of DIFFRACT based on the "old equations" has been extensively verified and validated in previous publications [12, 13, 19, 20]. Here we compare results from the old and new formulations for two different fixed body configurations. We also present results for multiple moving bodies and compare these with other published data.

3.1 Validation of method for removing the irregular frequencies

3.1.1 A single vertical uniform cylinder

We first consider the case of a vertical cylinder, and comparison with the second order analytical solution in [21]. The cylinder has radius a = 1 m and extends to the bottom in water of depth 1 m. The theoretical solution for the location of the irregular frequencies is easy to obtain. The first few values associated with the first Fourier harmonic circumferentially (which would therefore affect the first order horizontal force), specified in terms of dimensionless wave number ka (where k is the wave number), are obtained from the zeros of the Bessel functions J_1 as: ka = 3.83170597, 7.01558667, 10.17346814, 13.32369194. Second order quantities based on products of first order effects (so-called "quadratic" terms) involve all Fourier harmonics; and therefore irregular frequencies can potentially affect these quantities at the zeros of all orders of Bessel function. For the second order problem, forces were obtained using the meshes in Fig. 3 (in which the radius of the outer boundary of S_{Fe1} is 2.10533 m) over the range $0 < ka < 4.0$. In the specified water depth the wave numbers which correspond to half the values of the irregular frequencies listed above are ka = 1.16535421, 1.84393604, 2.5731498, 3.33931087. It can be expected therefore that problems would arise in evaluation of the double frequency second order potential near these values of ka.

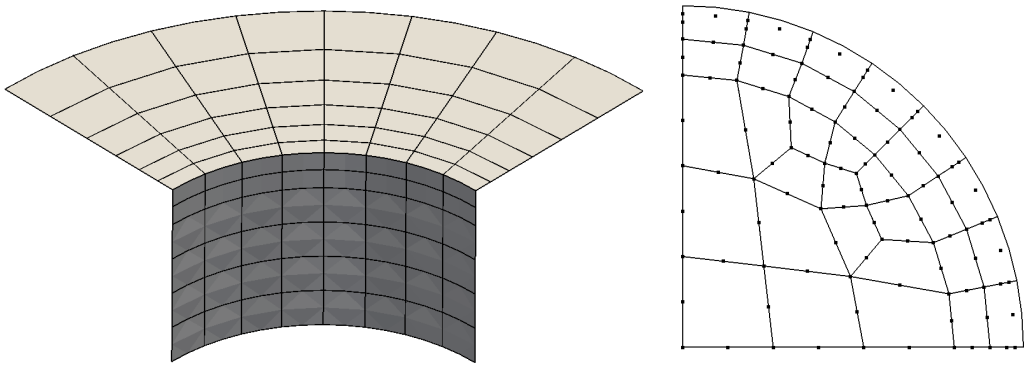

(a) (b)

Figure 3. Mesh used for second order analysis of vertical cylinder: (a) body surface and external free surface; (b) inner free surface

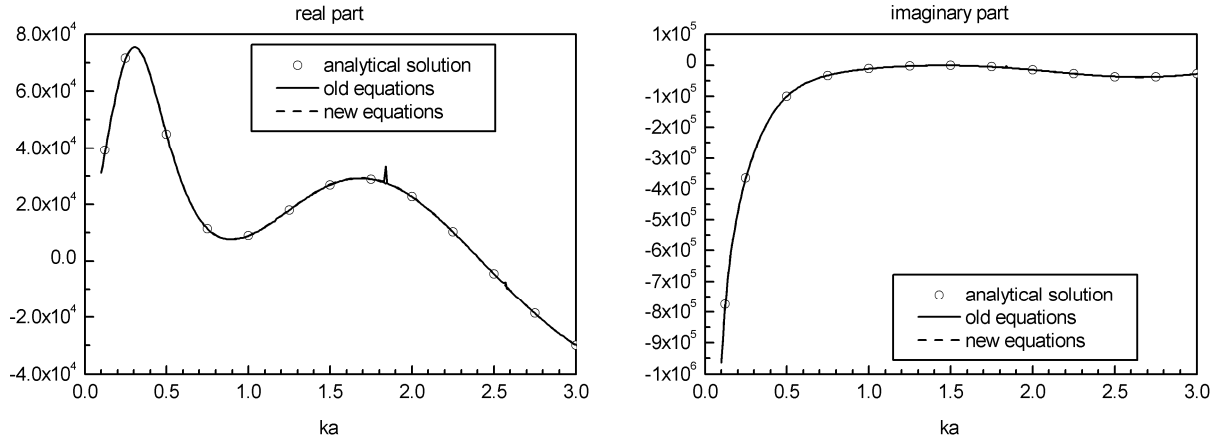

(a)

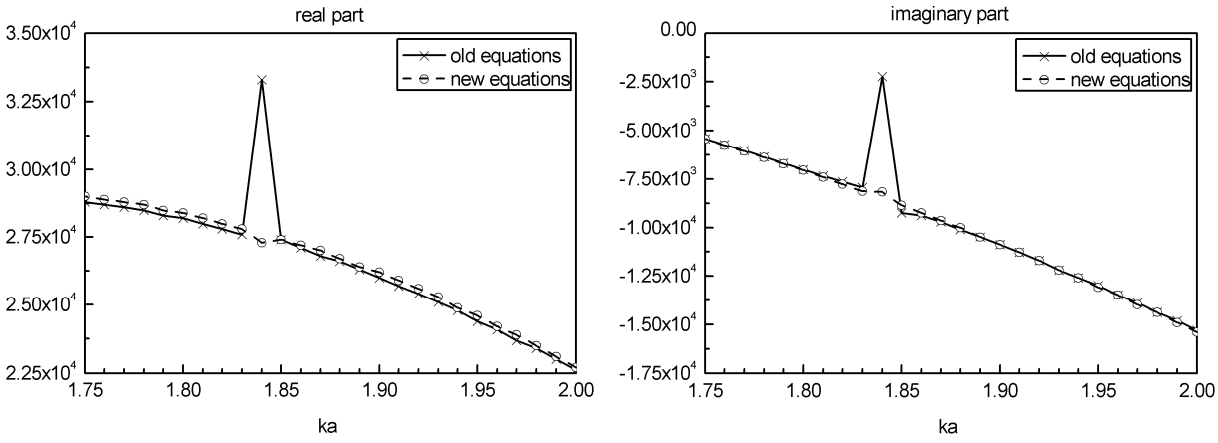

(b)

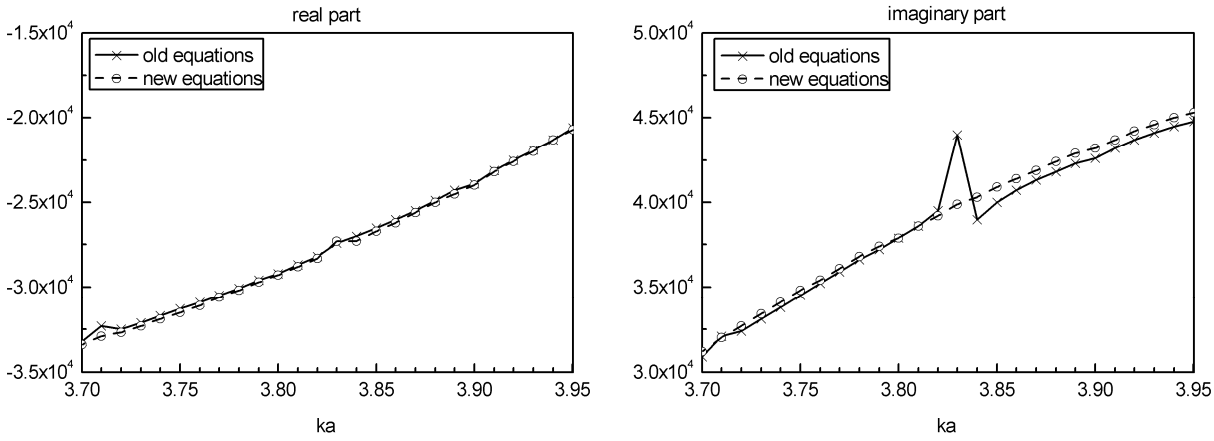

(c)

Figure 4. Second order horizontal force on a cylinder due to the 2nd order potential

Figure 4a compares the analytical solution for the 2nd order force (in Newtons) due to the 2nd order potential (real and imaginary parts) over the range $0 < ka < 3.0$, with results calculated from the original and new equations. Figure 4(b) shows the details near the irregular frequency associated with $ka = 1.84393604$. In Fig. 4(c) one can see irregularities associated with first order effects at $ka = 3.83170597$; and also with second order effects near $ka = 3.70348133$ (due to the second Fourier harmonic and the zero of J_2 having the value 14.79595178). The improvement in the results based on the new formulation is clear.

3.1.2 Second order forces on two fixed vertical cylinders

We next consider two vertical cylinders whose centre lines are $3a$ apart, in water of depth $3a$, a problem considered by Ghalayini and Williams [22]. In this case the first order horizontal forces are susceptible to irregularities at frequencies corresponding all of the Fourier modes, because the waves encountering one cylinder as a result of scattering by the other contain the full spectrum of harmonics symmetric about $\theta = 0$. Here we consider the second order problem, where again all these harmonics can contribute. It is easy to show that the lowest irregular frequencies correspond to $ka = 0.6293948494, 0.9638441312, 1.2850569034, \cdots$.

Figure 5 shows the general arrangement and the meshes employed (in the numerical model two planes of symmetry have been applied and the radius of the outer boundary of S_{Fe1} is 4.5a). The horizontal forces on each cylinder due to the second order potential are shown over the range $0 < ka < 1.5$ in Fig. 6(a), as calculated using the old and new equation formulations. These are for constant wave steepness $kH=0.2\pi$ (k is called k_0 in [22], and H is the incident wave height) and results are

nondimensionalized by $\rho g H \pi a^2/2$ (here ρ is the fluid density, g is the acceleration due to gravity). The figures may (with difficulty) be compared with the plots in [22], in which a much larger ordinate is used because other components of force are also plotted. The agreement appears to be satisfactory. Figure 6(b) shows expanded versions of these plots over the range of wave numbers close to that corresponding to the first irregular frequency given above. The improvement from using the new equations is again clear.

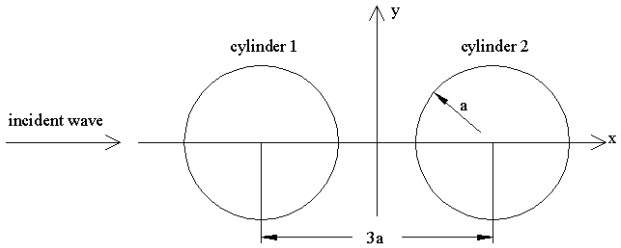

(a)

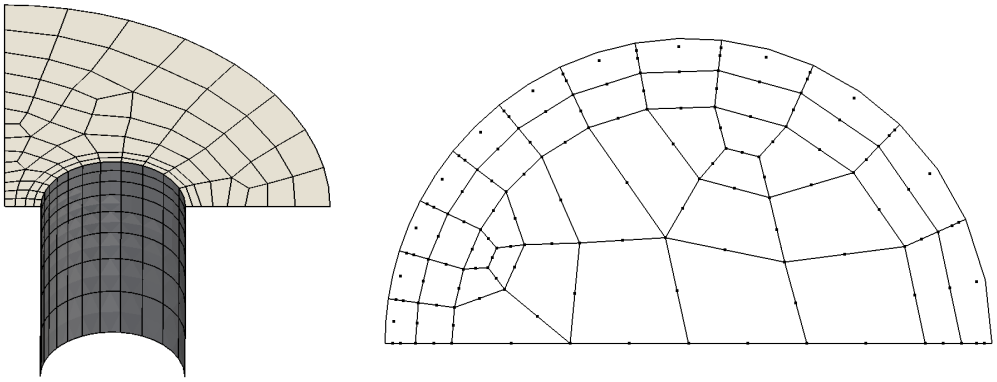

(b) (c)

Figure 5. General arrangement (a) and meshes (b, c) for the two-cylinder problem

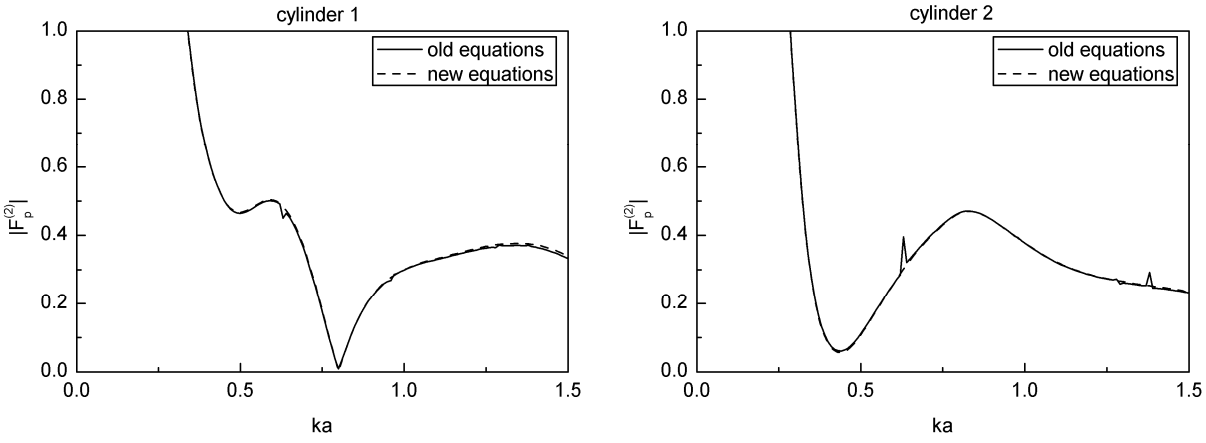

(a)

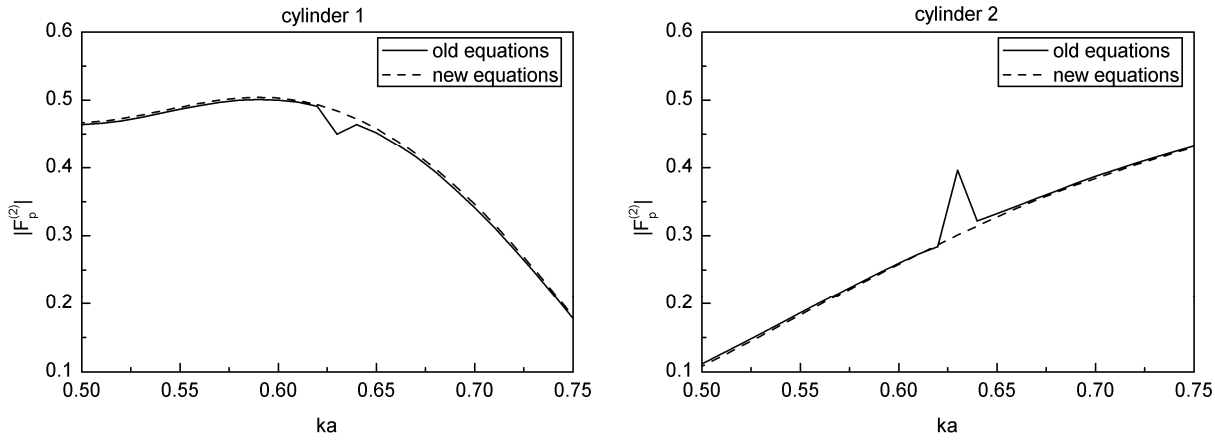

(b)

Figure 6. 2nd order force due to 2nd order potential (nondimensionalized by $\rho g H \pi a^2/2$)

3.1.3 Linear horizontal forces on a fixed box

This case concerns a fixed box having a rectangular waterplane area (length=1.125m, width=0.325m), and draft=0.125m. This corresponds to a configuration investigated in the SAFE OFFLOAD programme, for which results were obtained at model scale over a specified range of wave periods. The meshes used for the linear analysis are shown in Fig. 7. Although the shapes of some of the elements on the inner surface in Fig. 7(b) appear somewhat distorted, our experience is that satisfactory results are obtained. The results of surge and sway forces based on old and new equation are compared in Fig. 8 (here *A* is the incident wave amplitude). Again the irregular frequencies can be obtained by means of some simple analysis. They correspond to the wave periods indicated by vertical lines over the range of 0.25s < *T* < 0.3s in Fig. 8. The large number of irregular frequencies for this configuration is very striking. It may be clearly seen that, as expected, the irregular frequency effects that are triggered depend on the direction of the incident wave. The graphs show that the original equations provide results which to all intents and purposes are useless over substantial parts of the period range. The new equations, however, yield satisfactory results.

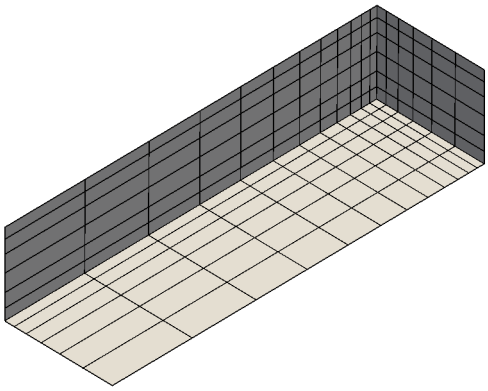

(a)

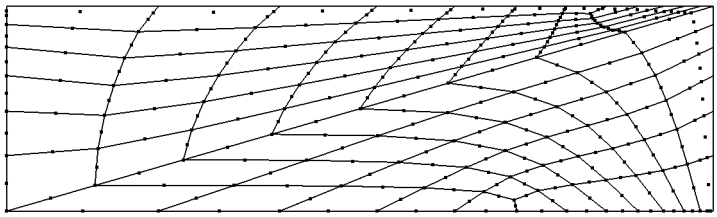

(b)

Figure 7. Meshes for rectangular box linear analysis: (a) body surface; (b) inner free surface

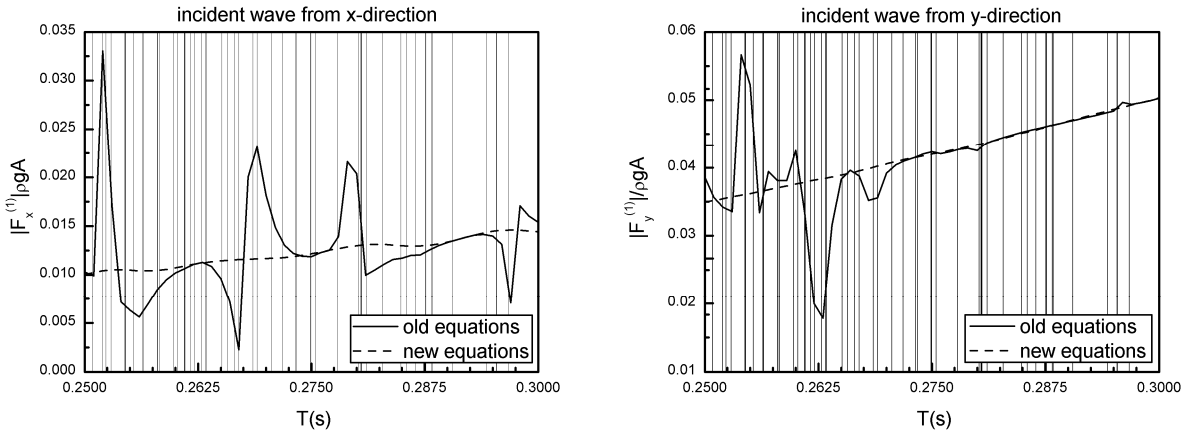

(a) (b)

Figure 8. Linear forces on a box: a) surge force in head seas; b) sway force in beam seas

3.2 Validation of analysis for multiple moving bodies: two free floating truncated cylinders

There are rather few published results for the radiation problem corresponding to two independently oscillating bodies, and fewer still (if any) for the second order forces on independently oscillating bodies. The former problem has been considered by Matsui and Tamaki

[23], who obtained results for a pair of bodies by a multiple scattering approach. In this, an axisymmetric boundary element source distribution was used to model each body. We here investigate the case of two freely floating truncated cylinders and compare the generalised added mass and damping matrices, and the responses, with the results given for this case in [23]. Figure 9 shows the general arrangement, and the body surface meshes for two different DIFFRACT models (coarse mesh 1 and finer mesh 2, using one plane of symmetry).

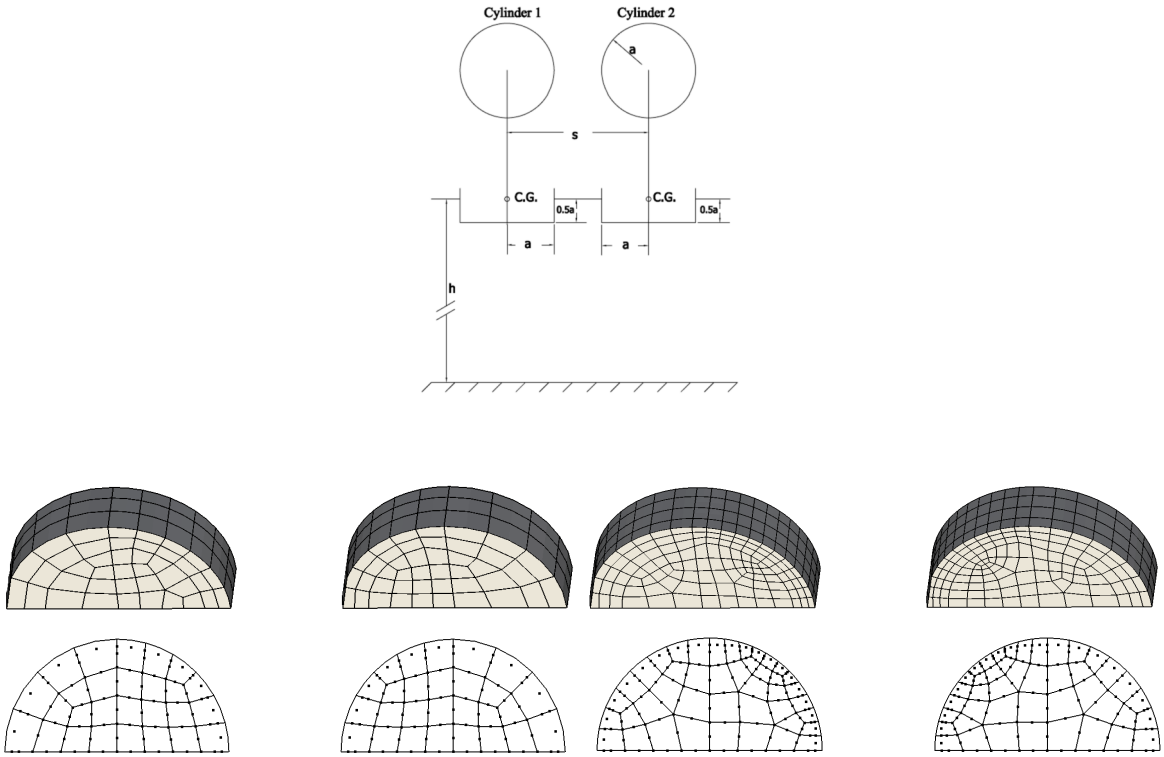

Figure 9. General arrangement and two meshes used for the pair of truncated cylinders

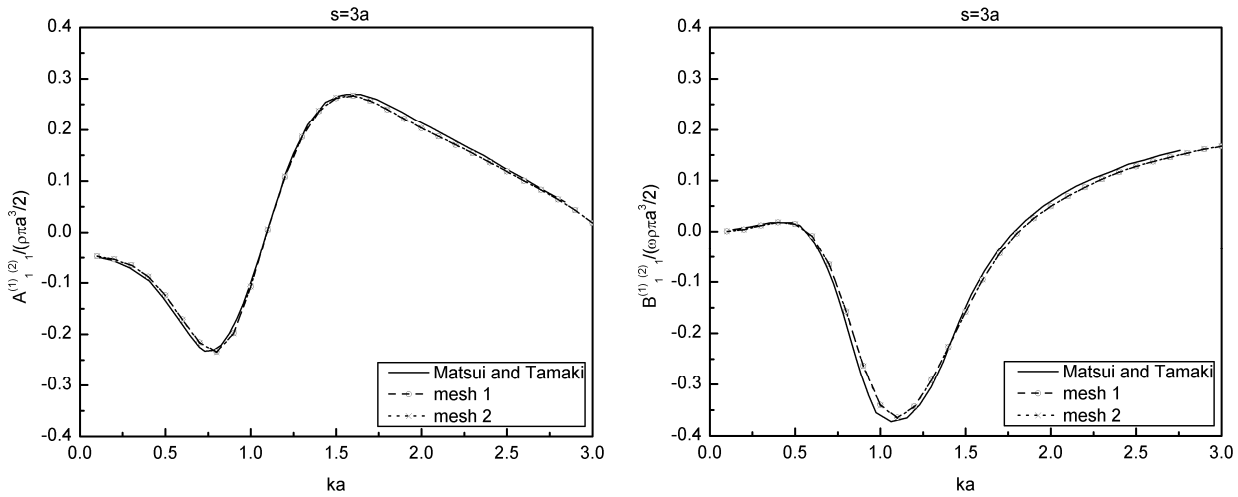

Figure 10. Coupled added mass and damping in surge for independently oscillating cylinders

Examples of cross coupling hydrodynamic terms are shown in non-dimensional form in Fig. 10. These are the added mass $A_{1\ 1}^{(1)(2)}$ and radiation damping $B_{1\ 1}^{(1)(2)}$, corresponding to the surge force on cylinder 1 due to surge motion of cylinder 2, for a centre-to-centre spacing s=3a. Results from the two meshes in Fig. 9 are almost indistinguishable. Comparison with values taken from the plots given in [23] shows very slight disagreement (possibly linked to the inaccuracy in reading off the published graphs), although the trends are very similar.

4. Configuration and numerical models of FLNG and LNG tanker

We now apply our boundary element model to one of the case studies investigated in the Safe Offload project. The two vessels are in a parallel configuration side by side, with a small gap of 4m between them. The water depth is 250 m. The geometry, inertia and hydrostatic properties of the FLNG are given in tables 1-2, and the corresponding properties for the tanker are in tables 3-4. The geometry of the tanker was simplified for this analysis. This was to enable the complex second-order problem of very closely spaced vessels such as these to be investigated in detail without incurring excessive computing times. A particular target of the simplification is to ensure that both the FLNG barge and the tanker are symmetric fore and aft. It is convenient then in the numerical modelling to make use of the existence of a plane of symmetry through the midships of both vessels. The geometry of the two vessels for meshing is therefore as shown in Fig. 11. The analysis is essentially based on the assumptions of potential flow. In order however to calculate realistic values of roll (and coupled sway) in freely-floating states, it is necessary to account for additional damping

due to viscous effects. We have used values provided by Noble Denton [24], as shown in table 5. This is in addition to the radiation damping automatically calculated by the diffraction code.

We stress the difficulty of the calculation we are attempting. We are unaware of any other authors who have included such a narrow gap compared to the size of the bodies themselves (4m versus 400m). Clearly any contamination of the solution from irregular frequencies would completely destroy the solution. Our extensive testing and comparisons to known analytic solutions [6] provides confidence in the quality of the results.

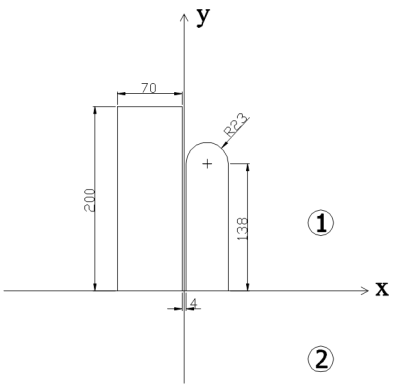

Figure 11. Configuration of FLNG and Tanker

Table 1. FLNG Principal Particulars

Length BP	400.0 metres
Breadth	70.0 metres
Depth to Main Deck	36.0 metres

Table 2. FLNG Mass Properties (Loaded Draft)

Mean Draft	21.254 metres
Displacement	610,000 tonnes
Vertical Centre of Gravity	22.4 metres
Metacentric Height (GM)	7.44 metres
Transverse Radius Gyration (K_{rr})	24 metres

Table 3. Tanker Principal Particulars

Length BP	276.0 metres
Breadth	46.0 metres
Depth to Main Deck	25.5 metres

Table 4. Tanker Mass Properties (Loaded Draft)

Mean Draft	11.4 metres
Displacement	97,000 tonnes
Vertical Centre of Gravity	16.0 metres
Metacentric Height (GM)	4.8 metres
Transverse Radius Gyration (K_{rr})	14.0 metres

Table 5. Added Additional damping in roll

FLNG	9.00E9 N-m/(rad/s)
Tanker	6.00E8 N-m /(rad/s)

The sizes and distributions of element meshes on boundary surfaces of the fluid domain are very important in the present simulations, especially for the second-order analyses. This has been examined in the context of two boxes in [6]. Satisfactory convergence of numerical results for the present second-order problem has been achieved up to $\omega \sim 0.85$ rad/s. Figures 12 and 13 show the meshes that have been used in the present computations, based on the experience gained in [6] for the simpler geometry of two rectangular boxes. In figure 13(a), the radius of the outer boundary of S_{Fe1} is 2500 m. On the other hand, to match the meshes on the body surface and obtain accurate results from the numerical integration, the meshes on the external free surface have to be limited to reasonable sizes (the meshes around the gap are shown in figure 13(b)). Comparing different meshes on the external free surface (Figure 3(a), 5(b) and 13), one finds that the size of meshed region S_{Fe1} may change dramatically for different configurations. This is related to the incident wave number, water depth and dimensions of the structure. For larger structures in deeper water, bigger meshed regions S_{Fe1} are needed to achieve converged results at higher wave frequencies: this is associated with the numerical treatment of the free surface forcing terms, described in [14].

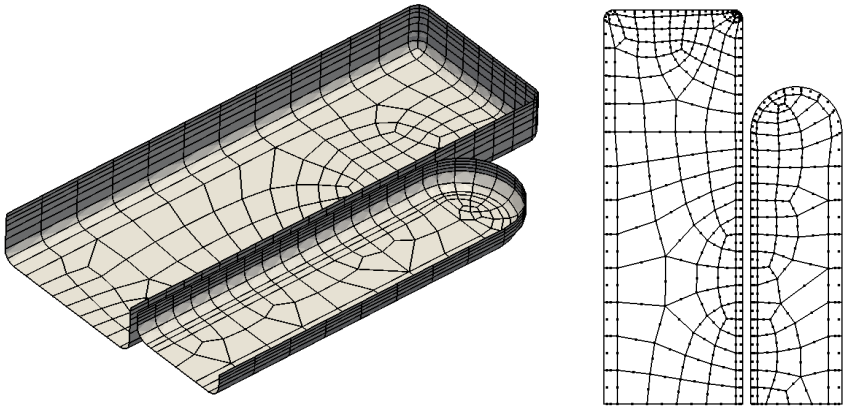

(a) (b)

Figure 12. Meshes on the body surface (a) and inner free surface (b)

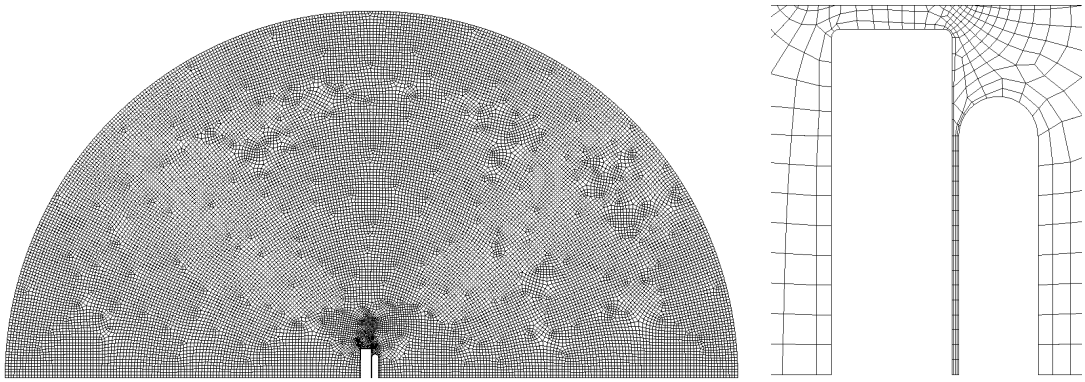

Figure 13. Meshes on the external free surface

5. Results

5.1 Motions and wave elevations in head seas

Both fixed and floating states are considered in the computations. The results are presented (for head seas in this sub-section, subsequently for the two beam sea cases) in the following order: first order motions; first order elevations; second order mean elevations; second order double frequency elevations. The amplitude of the incident wave is in all cases taken as 1.0 m. The translations and wave elevations are in metres, and the rotational motions are in degrees. In the figures showing wave elevations, the left hand plot corresponds to the vessels being fixed, and the right hand plot is for the case when the FLNG barge and the tanker both are free to respond independently. In the second order contribution of wave elevation with the vessels free, the contribution of second order motions is neglected. In the convention we have adopted here for head seas, waves are incident along the y-axis (see Fig. 11). In both this and in the subsequent beam sea cases, the wave elevation is calculated on the wall of FLNG barge, at its mid length 200m from each end, and the gap is 4m wide.

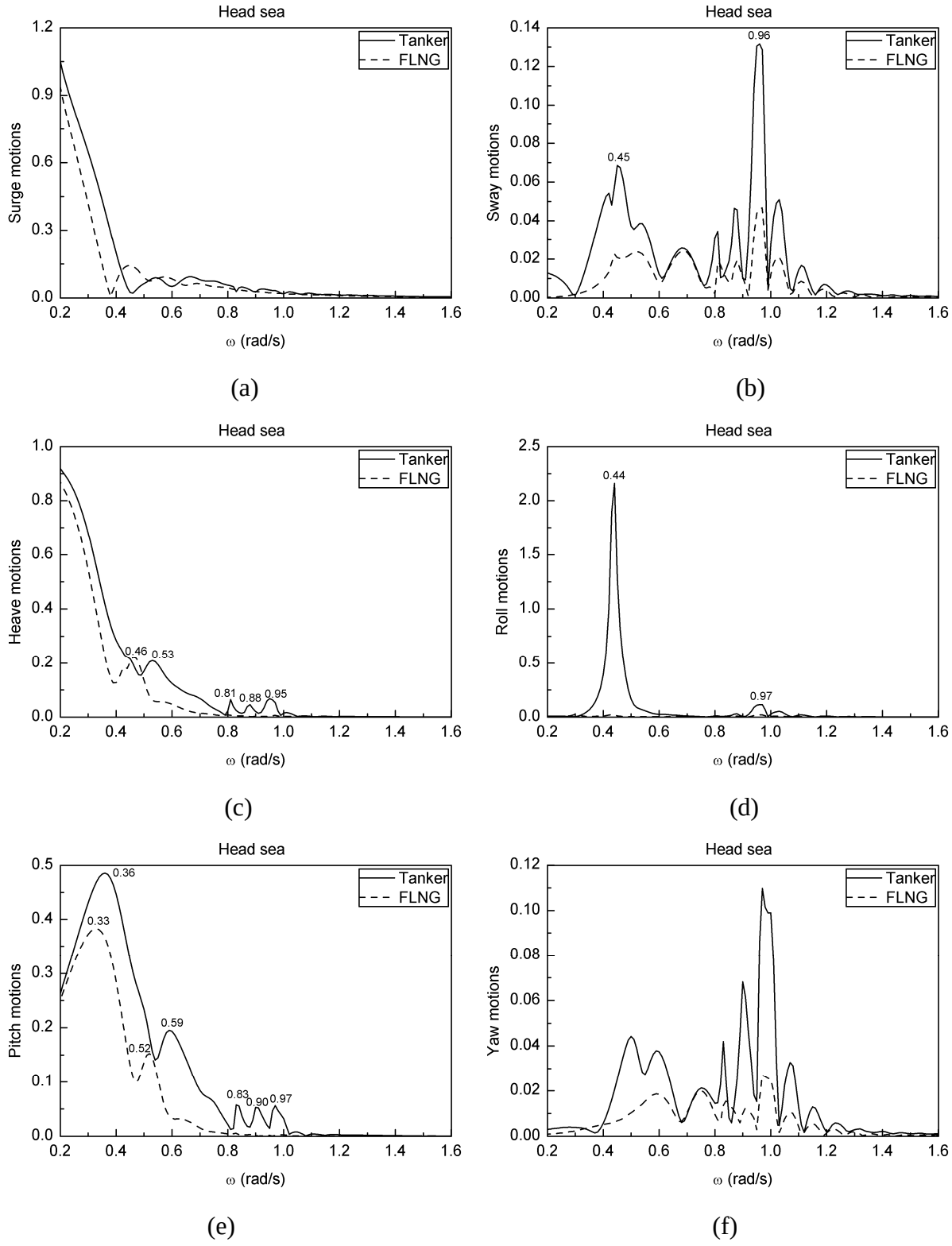

Figure 14. Surge, sway, heave, roll, pitch, yaw motion of Tanker and FLNG in head seas

In head sea cases, there are motions in the 6 degrees of freedom of each vessel. RAOs of the tanker and the FLNG in this configuration are shown in Fig. 14. Over the range of frequencies considered, the tanker usually has larger motions than the FLNG, because of the greater inertia of

the latter. The results are plotted at a frequency spacing of 0.01 rad/s and the frequencies of some predicted maximum amplitudes are identified by the numbers indicated alongside the peaks.

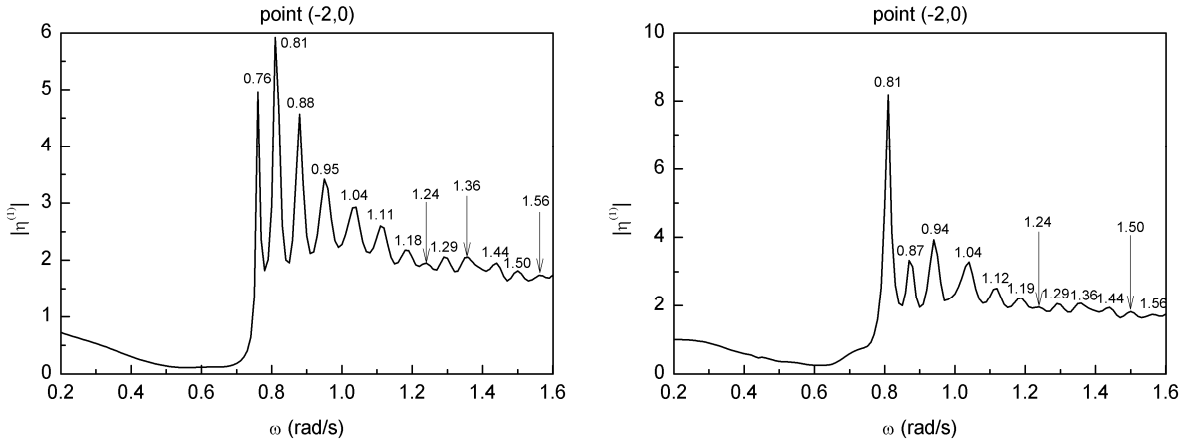

(a) **(b)**

Figure 15. First-order elevation at mid length along the FLNG in head seas: (a) fixed state; (b) freely-floating state

The first order elevations $|\eta|$ at mid length along the FLNG are shown in Fig. 15. In both the fixed and floating cases, there are many peaks, which correspond to the (*m*, 0) near-trapping modes described in [6]. In a (*m*, 0) mode, the free surface across the gap is flat; while the surface along the gap will include roughly 2*m*-1 half wave lengths (bearing in mind that the length of the gap is somewhat ill-defined for these two vessels of different lengths). By comparing the first-order elevations in fixed and freely-floating states in Fig. 15, one can observe a shift of the peak frequencies. The first peak at ω=0.76 rad/s which arises in the fixed state vanishes in the floating state. While in the fixed state the first-order elevations include just the effects of incident and diffracted potentials, in the floating states radiation potentials also contribute to the elevations. The latter appear to cause almost complete cancellation of the first peak at this central point (and also at all points along the gap), though a small residual at 0.76rad/s is just visible on the plot.

Figure 16 shows the mean second order elevations η_m plotted against the incident wave frequency. In these comparisons of mean elevations in the fixed and floating states, similar near-trapping phenomena and frequency shifts are found. At low frequencies, all the mean elevations at points half way along the gap are positive, corresponding to a mean set-up, whereas at high frequency a mean setdown occurs.

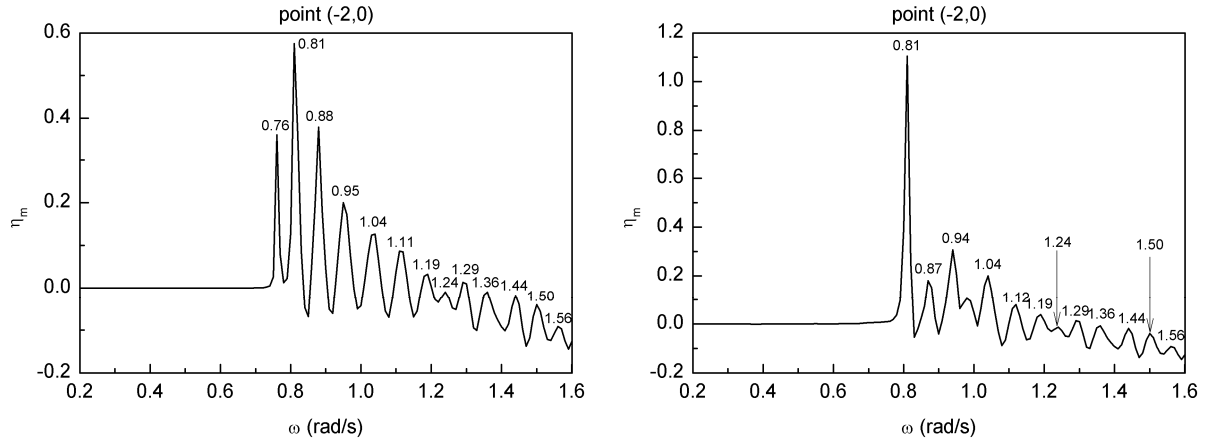

(a) **(b)**

Figure 16. Mean elevation at mid length along the FLNG in head seas: (a) fixed state; (b) freely-floating state

Figure 17 shows the modulus of the quadratic component (see §3.1.1) of the second order elevation $|\eta_q^{(2)}|$ plotted against the incident wave frequency. Again the results for the floating state miss the first peak at ω=0.76 rad/s. The corresponding modulus of the potential component $|\eta_p^{(2)}|$ (that due to the second order potential) is shown in Fig. 18. In this, a peak corresponding to the first peak in the first-order results is found in both fixed and floating states, at ω=0.38 rad/s. This of course is half of the frequency exciting the first order peak in the left hand plot of Fig. 16. The modulus of the total elevation $|\eta^{(2)}|$ is shown in Fig. 19.

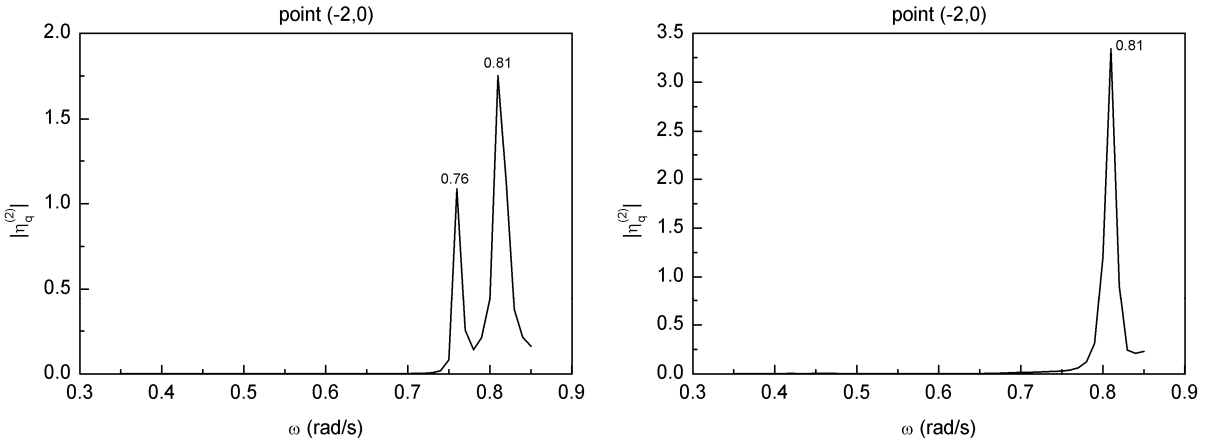

(a) **(b)**

Figure 17. Quadratic component of second-order elevations at mid length along the FLNG in head seas: (a) fixed state; (b) freely-floating state

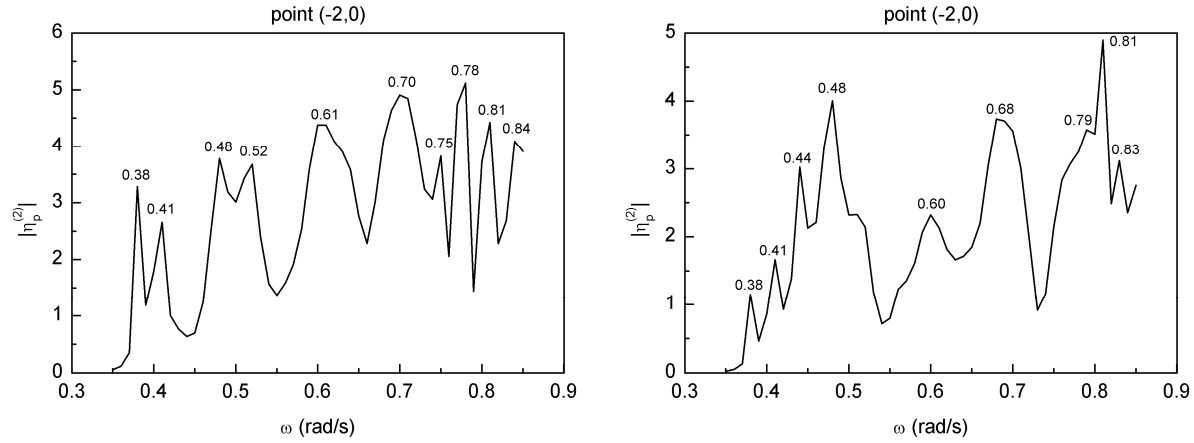

(a) **(b)**

Figure 18. Potential component of second-order elevations at mid length along the FLNG in head seas: (a) fixed state; (b) freely-floating state

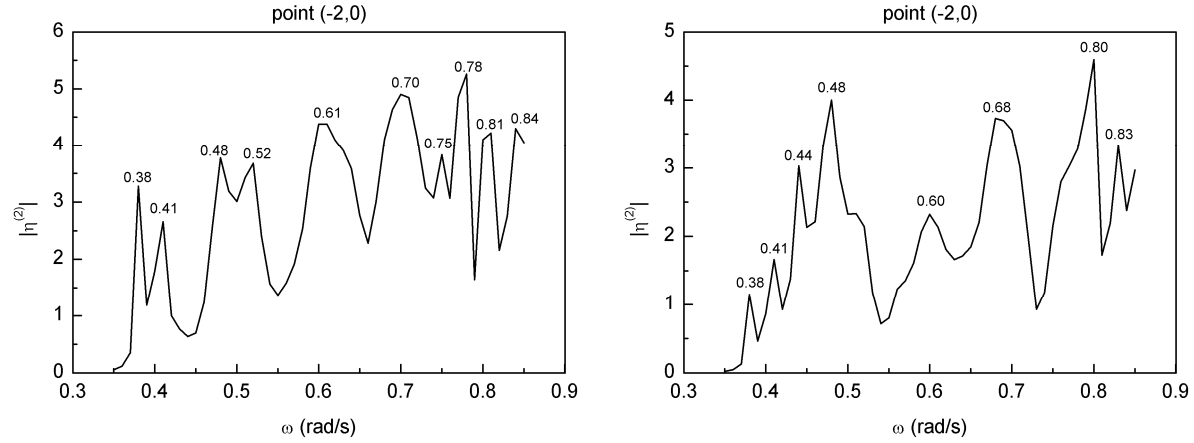

(a) **(b)**

Figure 19. Total second-order elevations at mid length along the FLNG in head seas: (a) fixed state; (b) freely-floating state

From Figs. 16-19 we conclude that the potential component predominates in the results for the second order elevation. Taken at face value, regular incident waves of amplitude 1m, if lying within a series of narrow frequency bands, are predicted to induce waves in the gap of some 4-5m amplitude. In practice, these theoretical predictions of amplitude cannot be expected to match experimental results precisely. Where the second order results are predicted to be as high as first order results, one can question the implications of the perturbation expansion. Furthermore, the

physical phenomenon is influenced by viscous effects leading to additional fluid damping, as discussed in the Conclusions and, for example, in Sun et al. [6] and Pauw et al. [4]. There is however no reason to doubt the predictions of violent motions at or near to the relevant wave frequencies identified here.

5.2 Motions and elevations in beam sea-1

This case (i.e. waves in the negative *x*-direction in Fig. 11) corresponds to the tanker being situated on the exposed (upwave) side of the FLNG. In both beam sea cases, there are motions in 3 degrees of freedom of each vessel, due to the symmetry of the problem. The associated RAOs of the tanker and FLNG in the beam sea-1 configuration are shown in Fig. 20. It is worth mentioning that larger roll motions are found here than in [25], because more frequencies have been calculated: the frequency spacing is 0.01rad/s here compared with 0.05rad/s in [25].

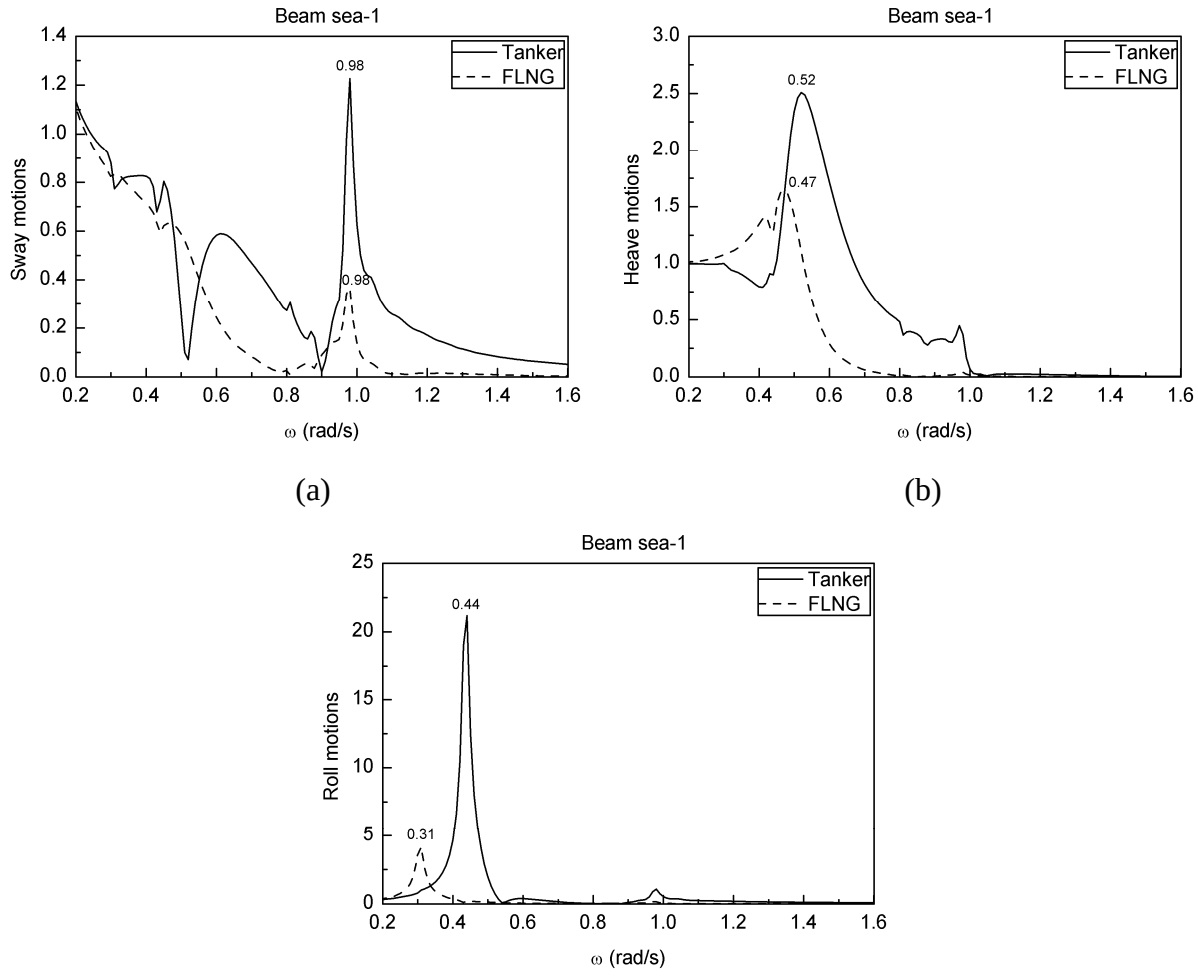

Figure 20. Sway, heave, and roll motions of tanker and FLNG in beam sea-1

Similar to the elevations in the head sea case, near-trapping phenomena and frequency shifts are found, as seen in Fig. 21. In the floating state, some small wiggles arise at low frequencies (see Fig. 21(b)). The first hump at ω=0.43 rad/s corresponds to the peak in the roll motion of the tanker (see Fig. 20(c)). The second hump at ω=0.52 rad/s corresponds to the peak in the heave motion of the tanker (see Fig. 20(b)).

The implications of these results, particularly for roll, are rather dramatic – for a 14s incident wave of 1m amplitude, a roll amplitude of 23° is predicted for the tanker. Whilst at this frequency, there is virtually no roll for the FLNG barge, long period swell with a 20s period would induce a 5° roll motion of the FLNG barge, potentially large enough for LNG production to have to cease. Both scenarios might occur for an FLNG production facility located off west Africa and excited by swell from the Southern Ocean.

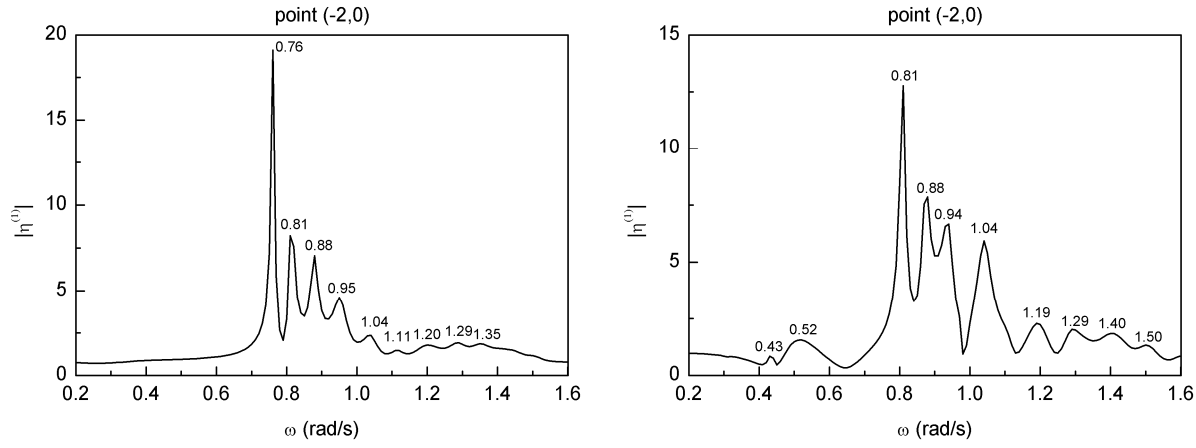

(a) **(b)**

Figure 21. First-order elevations at mid length along the FLNG in beam sea-1: (a) fixed state; (b) freely-floating state

Figure 22 shows the comparison of the mean elevation in the two states. Similar near-trapping phenomena and frequency shifts are found as above. There are fewer wiggles at high frequencies than in the head sea case.

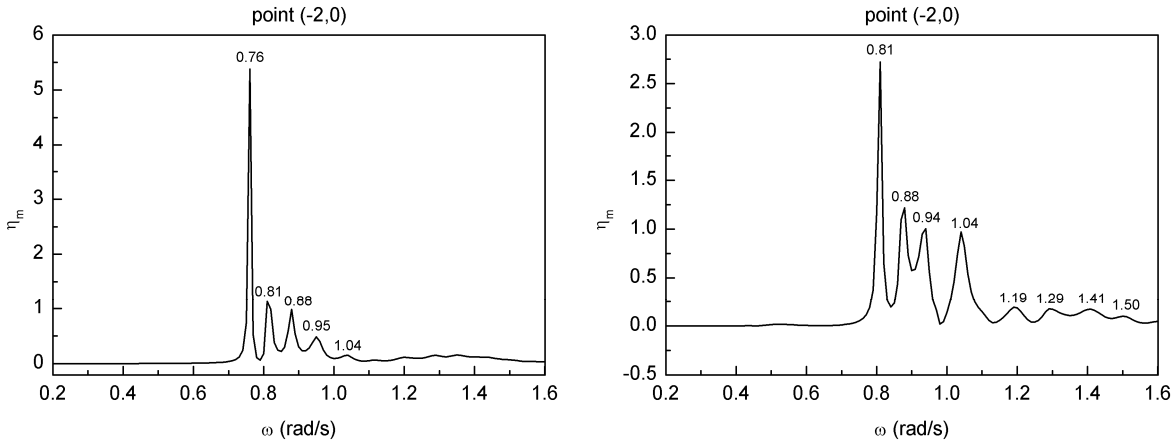

(a) **(b)**

Figure 22. Mean elevations at mid length along the FLNG in beam sea-1: (a) fixed state; (b) freely-floating state

Figures 23 and 24 show the amplitudes of the quadratic and potential components of the second order elevation, and Fig. 25 shows the total, in each case plotted against incident wave frequency. Similar near-trapping phenomena and frequency shifts are found. Significant cancellations are found between the quadratic and potential components in both fixed and floating states. At low frequencies in the fixed case (0.3-0.7 rad/s), the potential components again dominate the others. At 0.76 rad/s in the fixed case, however, the quadratic component predominates. At 0.81 rad/s in the fixed case, the potential component is the larger one. In the floating case, the potential component always predominates. The peaks in the total second order elevation at low frequencies become comparable to the peak value at 0.81 rad/s.

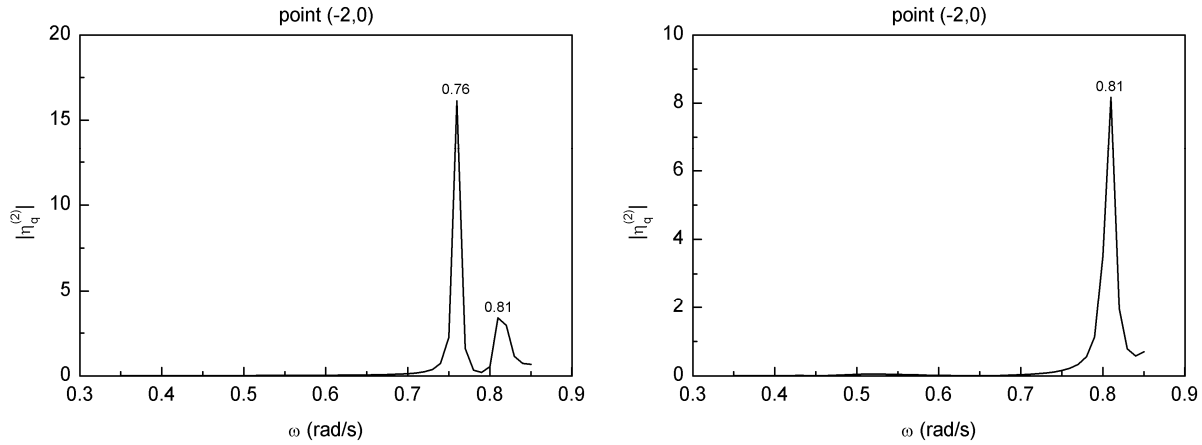

(a) **(b)**

Figure 23. Quadratic component of second-order elevations at mid length along the FLNG in beam sea-1: (a) fixed state; (b) freely-floating state

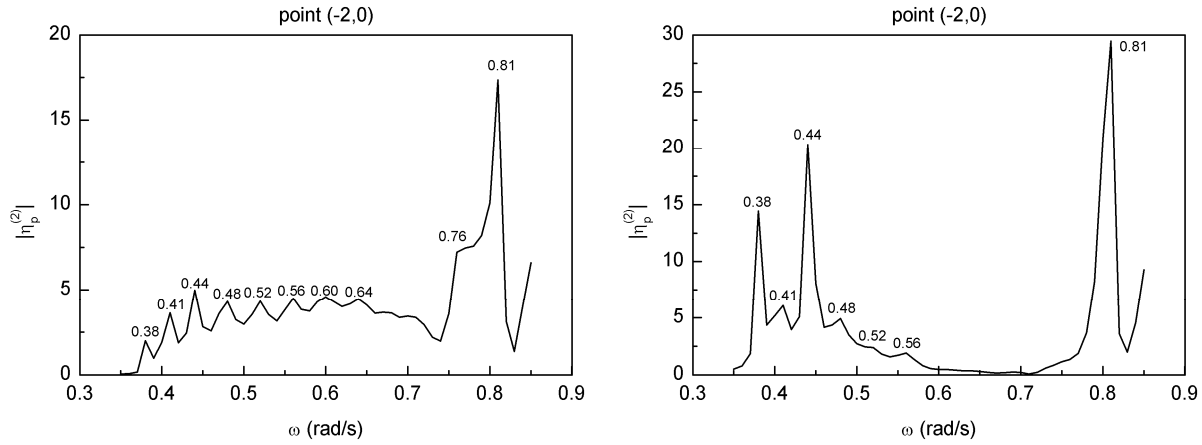

(a) **(b)**

Figure 24. Potential component of second-order elevations at mid length along the FLNG in beam sea-1: (a) fixed state; (b) freely-floating state

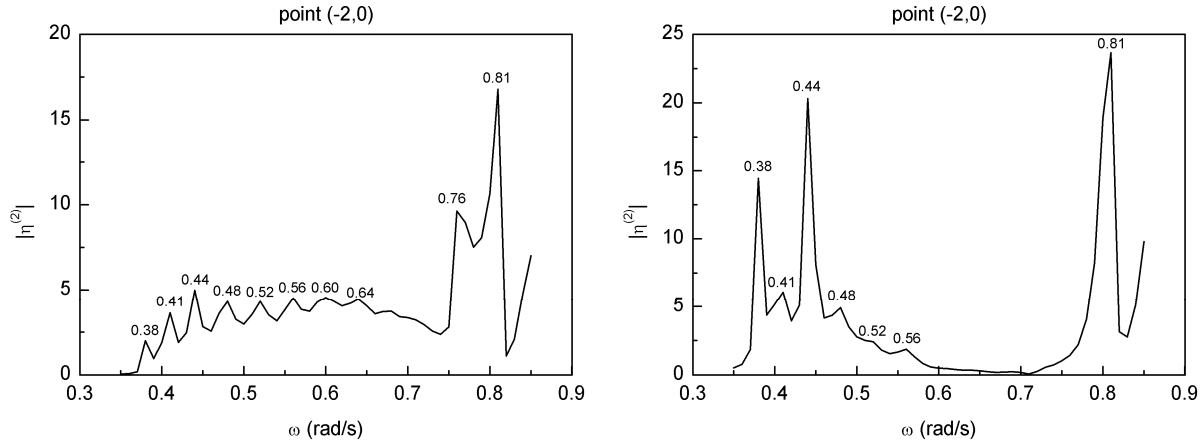

(a) **(b)**

Figure 25. Total second-order elevations at mid length along the FLNG in beam sea-1: (a) fixed state; (b) freely-floating state

5.3 Motions and elevations in beam sea-2

This configuration (i.e. waves in the positive *x*-direction in Fig. 11) corresponds to the tanker on the sheltered side (downwave) of the FLNG. The associated RAOs are shown in Fig. 26. Again larger roll motions are found than in [25], because of the smaller frequency increment used here. The peak heave and roll motions of the tanker are not as large as in the beam sea-1 case due to the sheltering effect of the FLNG.

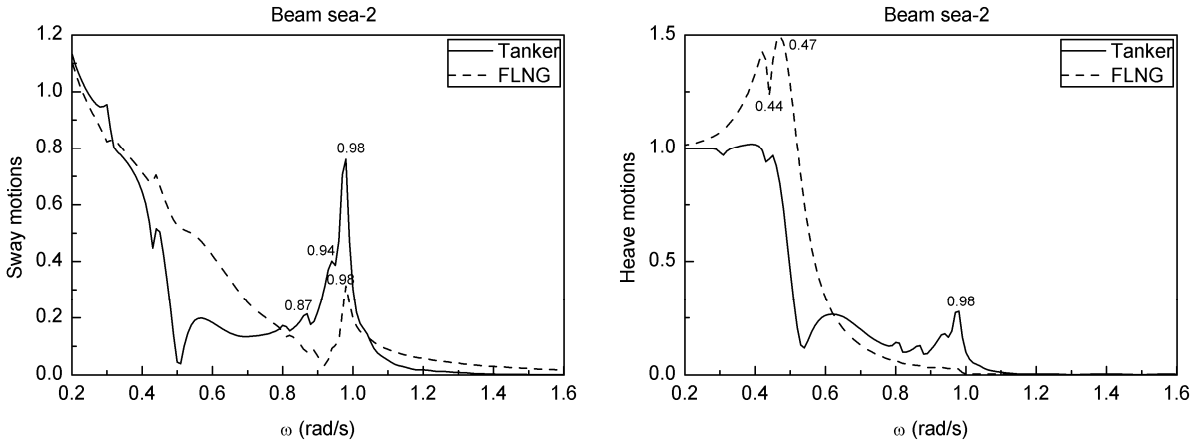

(a)

(b)

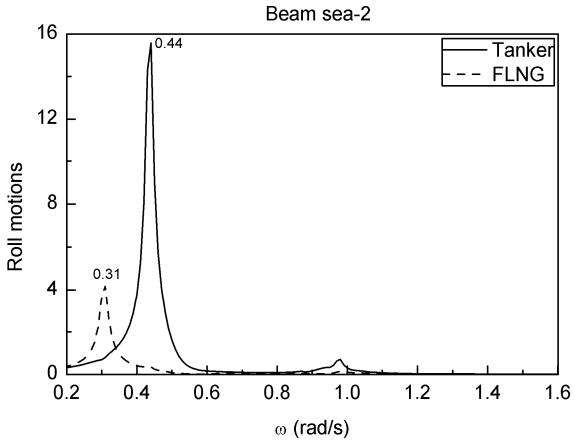

(c)

Figure 26. Sway, heave and roll motion of tanker and FLNG in beam sea-2

First order elevations for this case are shown in Fig. 27. As in the beam sea-1 case, near-trapping phenomena and frequency shifts are found. In the floating state, the wiggles arising at low frequencies (see Fig. 27(b)) are not as significant as in the beam sea-1 case, because the heave and roll motions of the tanker are lower at the peak frequencies.

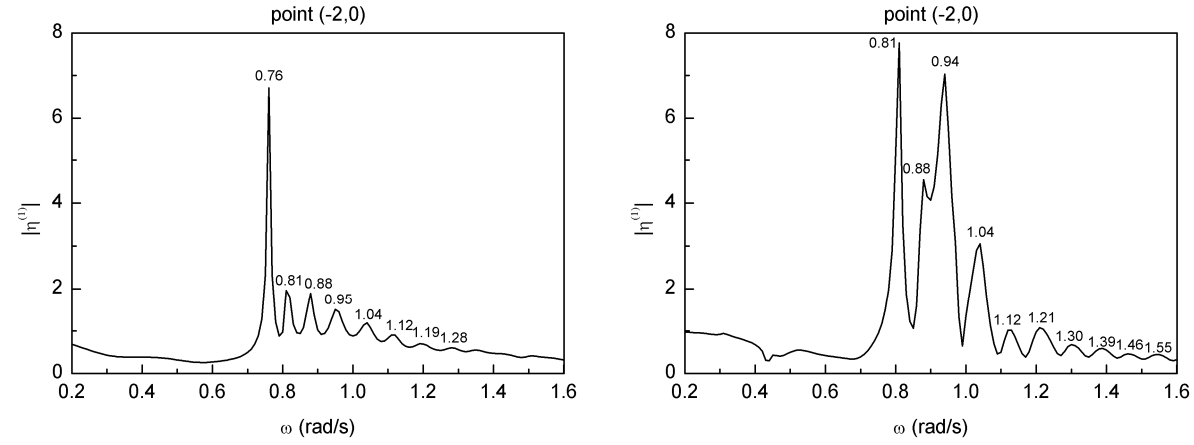

(a) **(b)**

Figure 27. First-order elevations at mid length along the FLNG in beam sea-2: (a) fixed state; (b) freely-floating state

In the comparisons of mean elevations in the two states, shown in Fig. 28, similar near-trapping phenomena and frequency shifts may be seen. The mean elevations at high frequencies tend to almost zero, with some very small wiggles.

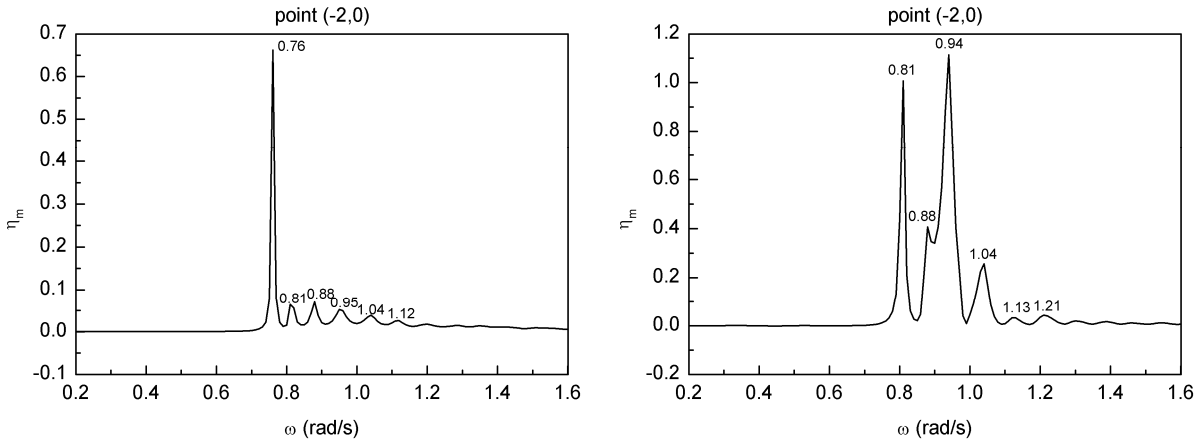

(a) **(b)**

Figure 28. Mean elevations at mid length along the FLNG in beam sea-2: (a) fixed state; (b) freely-floating state

Figures 29 and 30 show the amplitudes of the quadratic and potential components of the second order elevation, and Fig. 31 shows the total. Similar near-trapping phenomena and frequencies are found. From these results, we can conclude that the potential component predominates in both fixed and floating cases. Comparing the peak values of the quadratic component, potential component and total elevation, almost complete cancellation between the quadratic and potential components can be seen. It is of interest that the largest peak elevation for the floating case in Fig. 31(b) is obtained at 0.38 rad/s, which corresponds to half the frequency of the first peak in the first order elevation for the fixed case (see Fig. 27(a)).

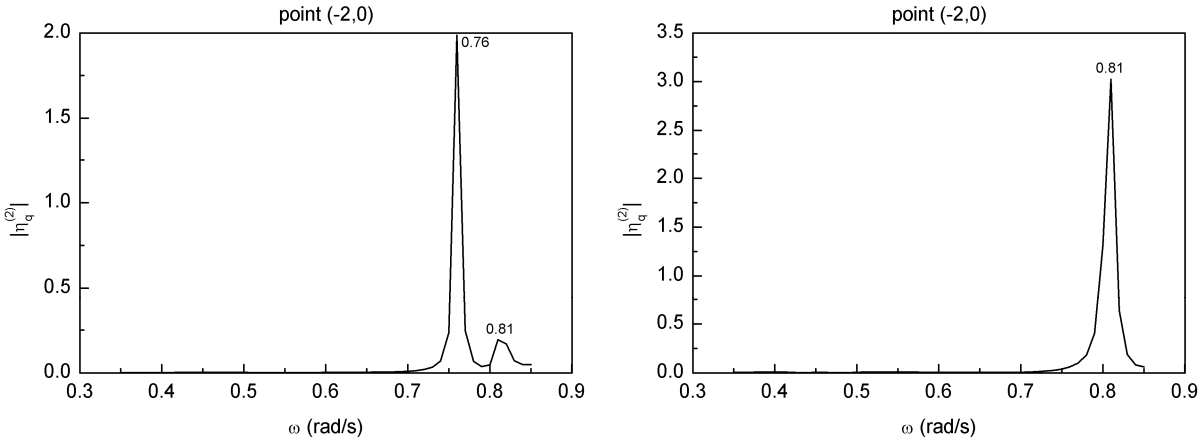

(a) **(b)**

Figure 29. Quadratic component of second-order elevations at mid length along the FLNG in beam sea-2: (a) fixed state; (b) freely-floating state

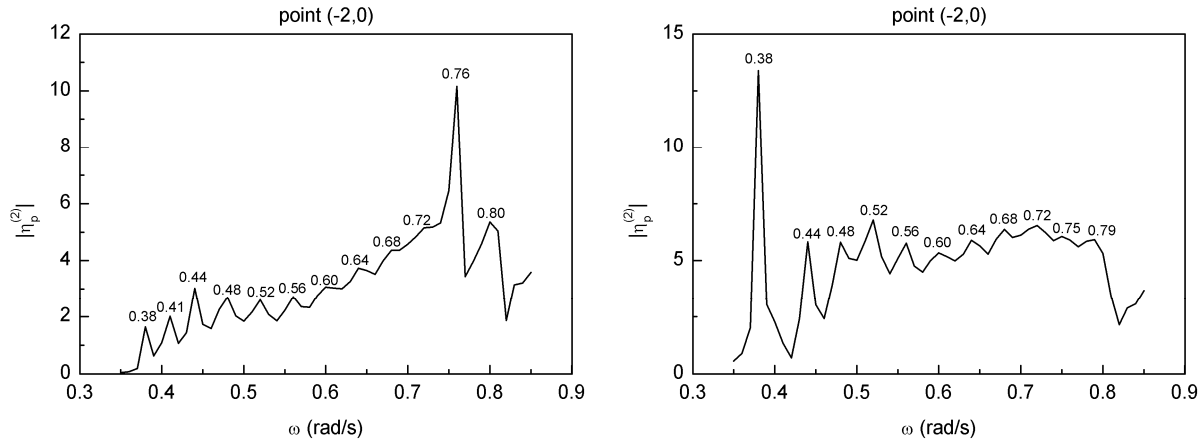

(a) **(b)**

Figure 30. Potential component of second-order elevations at mid length along the FLNG in beam sea-2: (a) fixed state; (b) freely-floating state

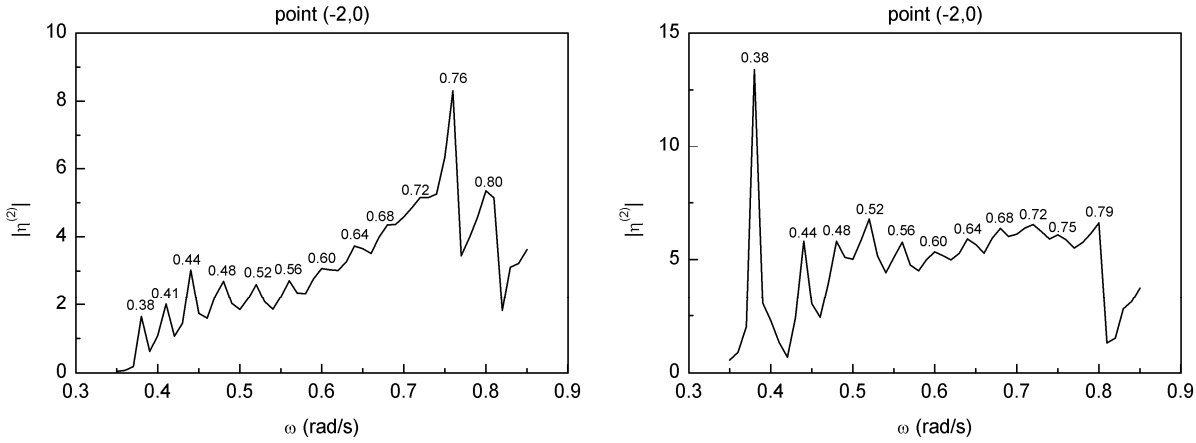

(a) **(b)**

Figure 31. Total second-order elevations at mid length along the FLNG in beam sea-2: (a) fixed state; (b) freely-floating state

6. Conclusions

The aim of this paper is to illustrate the significant wave interaction effects associated with a practical configuration of FLNG vessel with a tanker in a side-by-side arrangement at very close spacing. The results suggest that very high localised free surface elevations can occur in the gap at a set of discrete wave frequencies. The analyses have been undertaken with fine meshes of quadratic elements, which capture the intense fluid motions within the gap between the vessels.

Investigations have been conducted for the vessels free to move independently, as well as for the case when they are fixed. In the latter case there is an additional peak in the linear frequency response of the wave elevation in the gap, at a lower frequency than that of the lowest large peak in the case of freely moving vessels. This is observed in both head and beam sea configurations. The lowest peak in the second order frequency response for the free surface in the gap, for both fixed and free cases, is at half the frequency of the lowest linear peak for the fixed body case. The largest peaks, both linear and second order, arise in beam seas with the tanker upwave of the FLNG (beam sea – 1). Unsurprisingly this is the case causing the largest heave motions of the tanker. These, however, occur at a heave resonant frequency (0.52 rad/s) well below the frequency of the first very large peak in the linear free surface elevation between the freely moving vessels (0.81 rad/s).

It must be recognised that the peaks in elevations predicted by these potential flow calculations would not necessarily match very closely the results from experiments: viscous effects can be expected to provide additional damping over and above that due to wave radiation. There is no reason, however, to suspect that the frequencies of the peaks would not be predicted well. Various attempts have been made by others to improve the calculation of the interaction effects by incorporating some fictitious damping into the potential flow models, with the damping parameter chosen empirically such as to provide a match with experimental data. The difficulty of this approach has been highlighted in [4]. It was found that fitting one quantity, such as motion response, led to a different value of damping parameter from what is obtained from another quantity, such as mean drift force. It may be that the most appropriate quantity would be the peak free surface elevation in the gap, and this is currently under investigation using experimental data obtained at Imperial College as part of the Safe Offload programme. This is unlikely to be conclusive, however, because in some of the experiments the measured peaks in the free surface elevation were higher than the potential flow predictions. Another difficulty should also be recognised: the unknown dependence of the fluid damping on the physical scale at which the vessels are modelled. Further numerical work based on solution of the Navier Stokes equations can be expected to shed light on this issue in due course.

As a practical point, we stress the magnitude of the free-surface and body motions which can be excited by small amplitude waves when two large vessels are in very close proximity. Even if the practical responses in the field are a factor of 2 or 3 smaller than our idealised results suggest, there are likely to be major problems associated with the design of LNG loading arms to cope with such large vessel motions, and violent wave motion within the gap could threaten both equipment and crew should water be thrown up above deck level.

Acknowledgements

This work was supported by the SAFE OFFLOAD project under EU Framework 6. The collaborative partners are Shell International Exploration and Production B.V., Instituto Superior Tecnico Lisbon, DHI, Det Norske Veritas A/S, Imperial College London, Lisnave Estaleiros Navais SA, Noble Denton Consultants Ltd, Ocean Wave Engineering Ltd, and Oxford University. The EU project is linked to a JIP supported by ABS, Bluewater, Daewoo, Petrobras, SBM and StatoilHydro.

Support from the National University of Singapore during the later stages of the work is gratefully acknowledged, as is the provision of facilities by the Oxford Supercomputing Centre.

References

[1] Hong, S.Y., Kim, J.H., Cho, S.K., Choi, Y.R., Kim, Y.S. Numerical and experimental study on hydrodynamic interaction of side-by-side moored multiple vessels. Ocean Engineering 2005;32;783–801.

[2] Koo, B.J., Kim,M.H. Hydrodynamic interactions and relative motions of two floating platforms with mooring lines in side-by-side offloading operation. Applied Ocean Research 2005; 27:292–310.

[3] Teigen, P., Niedzwecki, J.M. A computational study of wave effects related to side-by-side LNG offloading. In: Proceedings of the 16th International Offshore and Polar Engineering Conference, San Francisco, USA; 2006.

[4] Pauw, W.H., Huijsmans, R.H.M., Voogt, A. Advances in the hydrodynamics of side-by-side moored vessels. In: Proceedings of the 26th International Conference on Offshore Mechanics and Arctic Engineering, San Diego, USA; 2007.

[5] Kashiwagi, M. 3-D calculation for multiple floating bodies in proximity using wave interaction theory. In: Proceedings of the 17th International Conference on Offshore and Polar Engineering, Lisbon, Portugal; 2007.

[6] Sun, L., Eatock Taylor, R., Taylor, P.H. First- and second-order analysis of resonant waves between adjacent barges. Journal of Fluids and Structures 2010; 26: 954-978.

[7] Molin, B. On the piston and sloshing modes of moonpools. Journal of Fluid Mechanics 2001; 430: 27–50.

[8] Newman, J. N., Sclavounos, P. D. The computation of wave loads on offshore structures. In: Proceedings of Fifth International Conference on the Behaviour of Offshore Structures BOSS `88 Trondheim, Norway; 1988.

[9] Lee, C.-H. and Newman, J.N. Computation of wave effects using the panel method. In: Numerical models in fluid-structure interaction, Ed. S. Chakrabarti, WIT Press, Southampton, 2004.

[10] Eatock Taylor, R., Chau, F.P. Wave diffraction theory - some developments in linear and non-linear theory. Transactions of ASME, Journal of Offshore Mechanics and Arctic Engineering 1992; 114: 185-194.

[11] Teng, B., Eatock Taylor, R. A BEM Method for the second order wave action on a floating body in monochromatic waves. Proceedings of International Conference on Hydrodynamics, ICHD94, Wuxi, China, 1994; p.274-281.

[12] Eatock Taylor, R., Kernot, M. P. On second order wave loading and response in irregular seas. In Advances in Coastal and Ocean Engineering, Vol. 5, Ed. P.L.-F. Liu, World Scientific 1999; p. 155-212.

[13] Zang, J., Wang, K., Eatock Taylor, R., Taylor, P. H. Second-order wave forces and free-surface elevation around a moored ship in steep uni-directional and spread waves. Proceedings of 4th International Conference on Marine Computational Fluid Dynamics, Royal Institution of Naval Architects 2005; p.53-58.

[14] Chau, F.P. The second order velocity potential for diffraction of waves by fixed offshore structures. Ph.D. thesis, University of London. Department of Mechanical Engineering, University College London, Report OEG/89/1; 1989.

[15] Zienkiewcz, O. C., Taylor, R. L. The finite element method for solid and structural mechanics. Butterworth-Heinemann; 2005.

[16] Brown, D.T, Eatock Taylor, R., Patel, M.H. Barge motions in random seas - a comparison of theory and experiment. Journal of Fluid Mechanics 1983; 129: 385-407.

[17] Sun, L., Teng, B., Liu, C. F. Removing irregular frequencies by a partial discontinuous higher order boundary element method. Ocean Engineering 2008; 35: 920–930.

[18] Subia S.R., Ingber M.S., Mitra A.K. A comparison of the semi-discontinuous element and multiple node with auxiliary boundary collocation approaches for the boundary element method. Engineering Analysis With Boundary Elements 1995; 15: 19-27.

[19] Zang, J., Gibson, R., Taylor, P. H., Eatock Taylor, R., Swan, C. Second order wave diffraction around a fixed ship-shaped body in unidirectional steep waves. Transactions of ASME, Journal of Offshore Mechanics and Arctic Engineering 2006; 128: 89-99.

[20] Walker, D. A. G., Eatock Taylor, R., Taylor, P. H., Zang, J. Wave diffraction and near-trapping by a multi-column gravity based structure. Ocean Engineering 2008; 35: 201-229.

[21] Eatock Taylor, R., Hung, S. M. Second order diffraction forces on a vertical cylinder in regular waves. Applied Ocean Research 1987; 9: 19-30.

[22] Ghalayini, S. A., Williams, A. N. Nonlinear wave forces on vertical cylinder arrays. Journal of Fluids and Structures 1991; 5: 1-32.

[23] Matsui, T., Tamaki, T. Hydrodynamic interaction between groups of vertical axisymmetric bodies floating in waves, Proc. Int. Symposium on Hydrodynamics in Ocean Engineering, Trondheim, Norway 1981; Vol. 2, pp.817-836.

[24] Noble Denton Consultants Ltd. Design solution for LNG platforms. NDC Report No: L22198/NDC/JK, Safe Offload Document Identification Code 12-D-02-01; 2007.

[25] Eatock Taylor, R., Taylor, P. H., Sun, L. Comparison of analyses for FLNG-tanker combination. Appendix A of “Hydrodynamic analysis of representative platforms”, Safe Offload Report 35-D-1, 2008.

List of figures

List of tables